LOFAR observations of refractive scattering from substructure within a traveling ionospheric disturbance at mid-latitude.

[1]Gareth Dorrian, [2,3]Richard Fallows, [1]Alan Wood, [1]David R. Themens, [1]Ben Boyde, [4]Andrzej Krankowski, [3]Mario Bisi, [4]Bartosz Dąbrowski, [5]Christian Vocks

[1]Space Environment and Radio Engineering Group (SERENE), University of Birmingham, UK

[2]ASTRON, National Institute for Radio Astronomy, The Netherlands

[3]RAL Space, United Kingdom Research and Innovation, Science & Technology Facilities Council, Rutherford Appleton Laboratory, Harwell Campus, Oxfordshire, OX11 0QX, UK

[4]Space Radio-Diagnostics Research Center, University of Warmia and Mazury in Olsztyn, Olsztyn, Poland

[5]Leibniz-Institut für Astrophysik Potsdam (AIP), Potsdam, Germany

Corresponding author: Gareth Dorrian: g.dorrian@bham.ac.uk

Key-points

A slow moving traveling ionospheric disturbance was detected exhibiting substantial internal substructure (on scales of ~ 20 km).

The propagation of the traveling ionospheric disturbance was estimated by several methods to be ~65 ms^{-1} in a NorthWesterly direction.

The substructure was larger than the Fresnel scale and generated refractive scattering and focusing of trans-ionospheric radio waves

Abstract

The large scale morphology and finer sub-structure within a slowly propagating traveling ionospheric disturbance (TID) are studied using wide band trans-ionospheric radio observations with the LOw Frequency ARray (LOFAR: van Haarlem, et al., 2013). The observations were made under geomagnetically quiet conditions, between 0400-0800 UT on 7 January 2019, over the UK. In combination with ionograms and Global Navigation Satellite System (GNSS) Total Electron Content (TEC) anomaly data we estimate the TID velocity to ~65ms^{-1}, in a NorthWesterly direction. Clearly defined substructures with oscillation periods of ~300 seconds were identified within the LOFAR observations of the TID, corresponding to scale sizes of ~ 20 km. At the geometries and observing wavelengths involved, the Fresnel scale is between 3-4 km, hence these substructures contribute significant refractive scattering to the received LOFAR signal. The refractive scattering is strongly coherent across the LOFAR bandwidth used here (25-64 MHz). The size of these structures distinguishes them from previously identified ionospheric scintillation with LOFAR in Fallows et

al., 2020 where the scale sizes of the plasma structure varied from ~500 m – 5 km.

Keywords: traveling ionospheric disturbance, ionospheric scintillation, Low Frequency ARray

1 Introduction

The signal received at a ground-based radio antenna from a distant natural radio source is a convolution of the source and a time- and frequency-dependent variability in amplitude and phase induced by scattering from plasma irregularities in the ionosphere. These effects can be broadly divided into diffractive scintillations (Singleton, 1970; Carrano et al., 2011) and refractive scattering (e.g. Forte, 2008), and chiefly depend on the scale sizes of the plasma irregularities and the wavelength of the radio waves received (Booker and Majidiahi, 1981; Booker, 1981). Observing the various manifestations of these signal variations therefore permits remote characterisation of ionospheric behaviour. When examining such variations in the High Frequency (HF) to Very High Frequency (VHF) band, with corresponding radio wavelengths ranging between ~100m – 1m, one can observe a wide variety of ionospheric scattering characteristics that span the refractive and diffractive domains (e.g. Fallows et al., 2014, 2020).

Ionospheric scintillation is the rapid variation (~1-second) in received amplitude and phase of radio waves transiting the ionosphere, due to diffractive scattering of the radio waves by small-scale plasma density features in the raypath (e.g. Wild & Roberts, 1956; Yeh & Liu, 1982, Tsunoda, 1985). Such plasma density features are highly structured (Bowman, 1981; Tsunoda, 1988; Muralikrishna et al., 2007) and rapidly alter the refractive index of the medium as a function of time and space, giving rise to the scintillations observed.

More specifically, the scintillation pattern is generated by many instances of constructive and destructive interference which occur between wavelets as they travel from the ionospheric scattering region to the observer. As the scattering region consists of many scatterers of different scale sizes which are moving across the raypath, some portion of the total power of the incoming radio wave will become reconfigured into a drifting scintillation pattern once it has crossed the space between the ionosphere and the observer and some will not. The scintillation pattern received by the observer is therefore a function both of ionospheric plasma scale size and distance between the observer and the ionosphere. The upper limit on scale size of the plasma scatterers which permit a fully developed scintillation pattern is called the Fresnel scale, or Fresnel limit, which is given by

$$F_D = \sqrt{2\lambda L} \quad (1)$$

where is the observed wavelength of the radio signal, and L is the distance from the observer to the ionospheric scattering region. As the population of plasma scatterers is in motion with respect to the observer the Fresnel scale can be converted to a Fresnel frequency, f_F, by

$f_F = \frac{\nu_p}{F_D}$ (2)

where v_p is the plane-of-sky propagation velocity of the scattering plasma as seen by the observer. Plasma structure scale sizes in the diffractive regime range from the Fresnel scale to approximately an order of magnitude below this value (Basu et al., 1998). For a given distribution of plasma scale sizes in the ionosphere, scintillation is more noticeable at HF and VHF (Groves et al., 1997). This is because lower frequencies correspond to larger Fresnel scale sizes, and hence the diffractive regime at larger Fresnel scales encompasses a greater proportion of the plasma scattering population.

Ionospheric scintillation is common at equatorial (e.g. Abdu et al., 1985) and auroral latitudes (e.g. Kinrade et al., 2012), but can be encountered at any location (Fremouw & Bates, 1971). It affects the accuracy of Global Navigation Satellite Systems (GNSS) (e.g. Kintner et al., 2007; Prikryl et al., 2015) which operate in the UHF range, and imposes some limitations on synthetic aperture radio astronomy observations (Hinder & Ryle, 1971). Thorough reviews of ionospheric scintillation and the underlying physical mechanisms are given by Aarons (1982), and Priyadarshi (2015), and a thorough review of ionospheric irregularities at all latitudes is given by Fejer & Kelley (1980).

Refraction through the ionosphere is caused by plasma irregularities which have scale sizes greater than the Fresnel scale. Under instances of sufficiently strong fluctuations in plasma density involving larger-scale plasma features, refractive scattering is the dominant source of variations observed in received signal power, and particularly signal phase (Booker & Majidiahi, 1981). Scattering effects of the ionosphere in general therefore pose challenges for low-frequency radio astronomy, and numerous authors have covered the subject in detail, including Magnum & Wallace (2015), and de Gasperin et al. (2018).

The very wide field-of-view, high time cadence, and large bandwidth (10-250 MHz) afforded by the LOw Frequency ARray (LOFAR: van Haarlem et al., 2013) make it an ideal instrument with which to investigate ionospheric plasma structures over a range of frequencies. Many previous ionospheric scintillation studies have tended to utilise one frequency or a small range of frequencies (e.g. Groves et al., 1997; Mitchell et al., 2005; RamaRao et al., 2006; Song et al., 2021) from GNSS or other systems. However, the scattering effect of ionospheric structures can be seen across wide bandwidths, particularly when observing natural radio sources (e.g. Fallows et al., 2014). In this paper we describe the observations of an ionospheric transient feature during a LOFAR observation of the natural radio sources Cygnus A (3C405), and Cassiopeia A (3C461), on 7 January 2019. Natural radio sources lend themselves well to ionospheric scintillation studies of this kind as they are inherently broadband emitters and thus permit observations of ionospheric influences on transited radio signals over a wide bandwidth. Cassiopeia A and Cygnus A are also two of the strongest natural radio source in the sky located outside the solar system.

Each LOFAR station consists of two arrays, a Low-Band Antenna (LBA)

array of dual-polarisation crossed dipole antennas suspended above the ground plane, and which cover the frequency range 10–90 MHz and a High-Band Antenna (HBA) array of tiles, each tile consisting of a phased array of 16 dual-polarisation bow tie antennas, which covers the range 110–270 MHz. In this paper we use data from the LBAs at the Irish and UK LOFAR stations (Station codes IE613 and UK608 respectively). IE613 is located near Birr in central Ireland at 53.10°N, 7.92°W; UK608 is located near Chilbolton in the south of England at 51.14°N, 1.43°W. Supplementary data from the Fairford ionosonde (FF051: 51.71°N, 1.79°E) from the Global Ionospheric Radio Observatory (GIRO) (Reinisch and Galkin, 2011) underlying the feature and GNSS Total Electron Content (TEC) data from the British Isles continuous GNSS Facility (BIGF) are also used. The GNSS TEC in particular provide a useful global context for the large scale morphology of the feature. LOFAR provides excellent high time resolution observations of the sub-structure within the feature, and the ionosondes enable the altitude of the feature to be approximated. Geophysical indices and data from suitably located ground-based magnetometers are also used to establish the overall space weather context at the time of these observations.

2 Observations

The data upon which this study is based were collected during LOFAR observations of 3C405, (Cygnus A: RA 19h59m28s and Dec. 40.73°) and 3C461 (Cassiopeia A: RA 23h 23m 24s and Dec. 58.82°) by IE613 and UK608, between 0400-0800 UT on 7 January 2019. These station locations are shown in Figure 8. The raw data for this observation can be obtained from the LOFAR long-term archive (https://lta.lofar.eu); observation ID L691956 under project LT10_006. From the perspective of both LOFAR stations, the radio sources were observed to rise in elevation and rotate clockwise in azimuth during the observing window (See Figure 7). A summary of the observing parameters is given in Table 1, showing the event onset and event end times for the two radio sources and the two LOFAR stations used. All times henceforth are given in UT.

Given that the observation took place over a 4-hour window, the significant changes in elevation and azimuth of both sources was reflected in a general increase in received intensity from the radio sources over all observing frequencies during the window. It was therefore necessary to remove the time-of-day dependence from the received signal power for the whole dataset. This was achieved by dividing the data in each sub-band channel by a fitted 3rd order polynomial. Removal of RFI noise spikes was achieved by median filtering of each channel in a sliding window of 50 data points, corresponding to ~0.5-seconds, and finding the standard deviation. Data points exceeding a 5 threshold within this window were removed.

Observation	Cassiopeia A Elevation	Cassiopeia A Azimuth	Cygnus A Elevation	Cygnus A Azimuth	Notes

UK608LBA					
	°	°	°	°	Observation Start
	°	°	Event not seen	Event not seen	Event onset, Cass. A
	°	°	Event not seen	Event not seen	Event end, Cass. A
	°	°	°	°	Observation End
IE613 LBA					
	°	°	°	°	Observation Start
			°	°	Event onset, Cyg. A
	°	°			Event onset, Cass. A
			°	°	Event end, Cyg. A
	°	°			Event end, Cass. A
	°	°	°	°	Observation End

Table 1. Observation summary and approximate event timings from LOFAR observations of Cassiopeia A and Cygnus A on 7 January 2019.

The LOFAR frequency coverage used here extends over 200 evenly spaced subbands of 195.3125 kHz, from 24.99-63.86 MHz. Note that the mininmum and maximum frequencies quoted are the mid-points of their respective channels. The extrema of the full LBA bandwidth are excluded as they are often contaminated with heavy RFI from HF signals trapped in the Earth-ionosphere waveguide at the low end and heavily filtered to exclude FM radio signals at the high end. Each channel is a 1-dimensional time series of received intensity, averaged to a time resolution of 0.01s.

Figures 1 and 2 show the observation data from the UK and Irish LOFAR stations respectively. RFI contamination still persists in a small number of channels and these are visible as horizontal streaks. In these plots the data have been averaged to 1-second across the full 4-hour observing window for both LOFAR stations and on both radio sources. The exact start and end times of the observation window are 04:00:00.0 to 07:59:59.5 respectively; the total number

of timestamps at 1-second resolution is 14455. In the top panel of Figure 1 it can be seen that the dynamic spectrum of Cygnus A from the UK station (hereafter UK-CygA) shows little obvious disturbances except near the very end of the observing window; the ionosphere along this raypath is relatively undisturbed. Dynamic spectra from other nearby LOFAR stations such as France (FR606: 47.4°N 2.2°E) also showed no significant activity during this time.

However, in the dynamic spectrum of Cassiopeia A (hereafter UK-CassA) from the same station, a distinct series of near-vertical signal fading and enhancement can be seen beginning at 05:25UT which continued for approximately 29 minutes, ending at 05:54UT. At 05:52UT a very similar feature appears in the dynamic spectra of Cygnus A as seen from the Irish LOFAR station (Figure 2, top panel, hereafter Irl-CygA). It continues for approximately 54 minutes, ending at 06:46UT. Fainter but similar looking structures appear briefly at the very end of the observation. Beginning at 06:32UT, in Cassiopeia A also on the Irish station (Figure 2, bottom panel; hereafter Irl-CassA), a series of signal enhancements, curving slightly to both earlier and later times at the lower frequencies, are seen shortly before a deep signal fade across all bandwidths which lasts for ~500 seconds. After signal power levels return there are a couple of fainter signal enhancements before the feature transits out of the raypath. The entire feature lasts some 49 minutes, ending at 07:21UT. Figures 1 and 2 are arranged in order of time of event onset, with the event first being seen in UK-CassA, then Irl-CygA, then Irl-CassA.

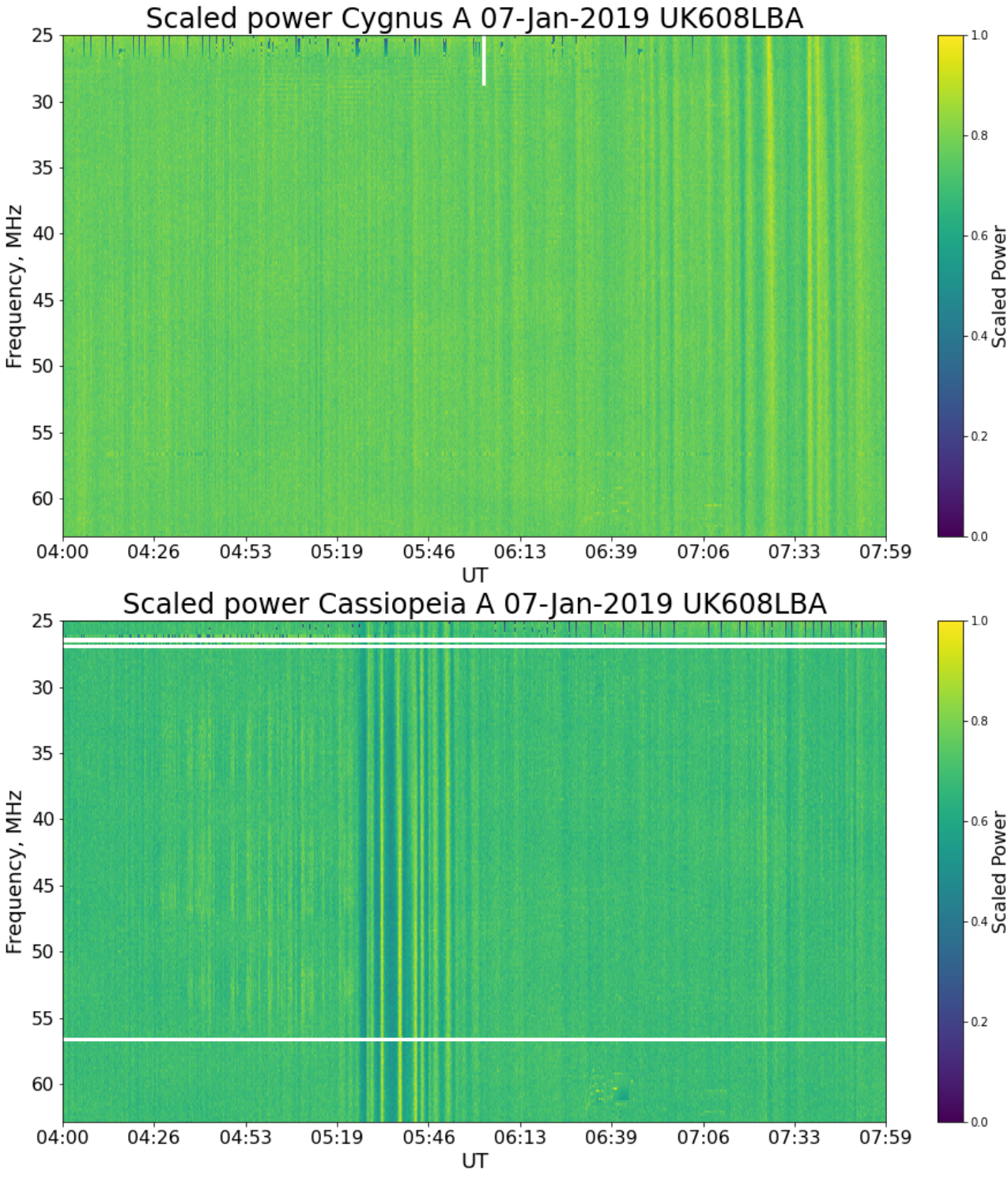
Scaled power Cygnus A 07-Jan-2019 UK608LBA
Frequency, MHz
25
30
35
40
45
50
55
60
04:00
04:26
04:53
05:19
05:46
06:13
06:39
07:06
07:33
07:59
UT
Scaled Power
0.0
0.2
0.4
0.6
0.8
1.0
Scaled power Cassiopeia A 07-Jan-2019 UK608LBA
Frequency, MHz
25
30
35
40
45
50
55
60
04:00
04:26
04:53
05:19
05:46
06:13
06:39
07:06
07:33
07:59
UT
Scaled Power
0.0
0.2
0.4
0.6
0.8
1.0

1. Dynamic spectra for the UK LOFAR station (UK608LBA) from 0400 to 0800 UT on 7 January 2019. The top panel shows the data collected from observations of Cygnus A and the bottom panel shows likewise from Cassiopeia A. The horizontal streaks are RFI. Event onset in Cassiopeia A is at 0520 UT.

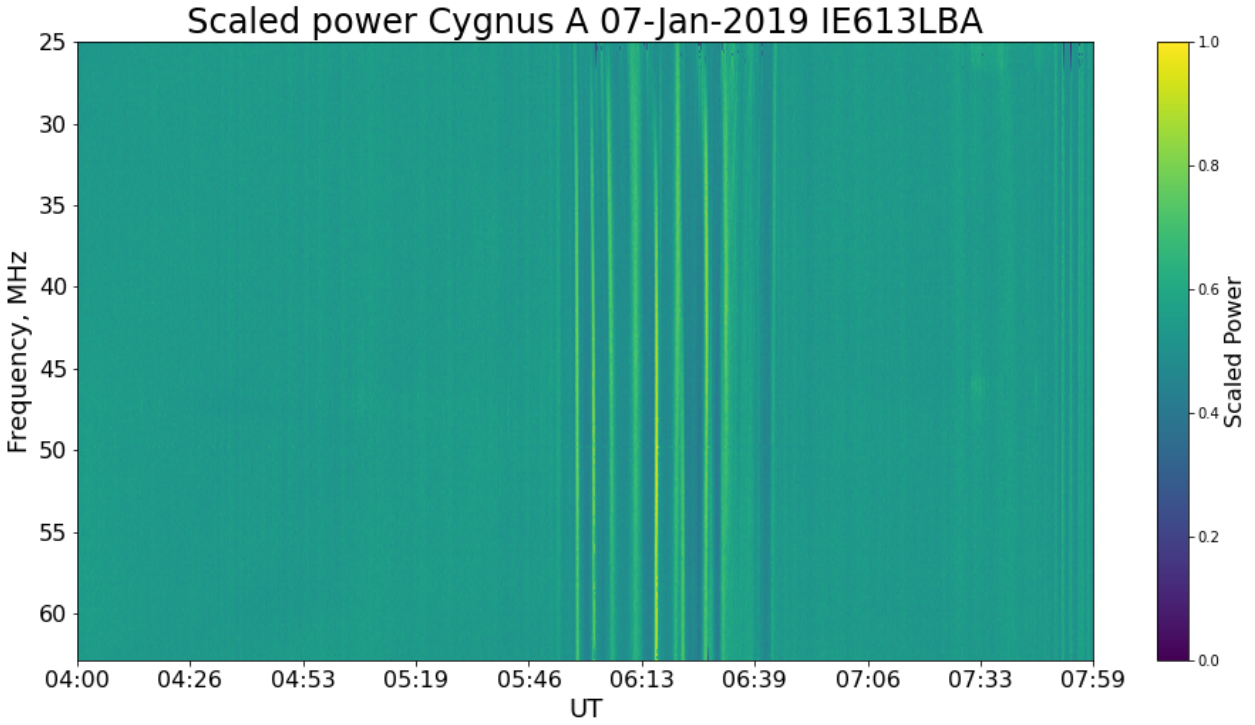
Scaled power Cygnus A 07-Jan-2019 IE613LBA
Frequency, MHz
25
30
35
40
45
50
55
60
04:00
04:26
04:53
05:19
05:46
06:13
06:39
07:06
07:33
07:59
UT
Scaled Power
0.0
0.2
0.4
0.6
0.8
1.0

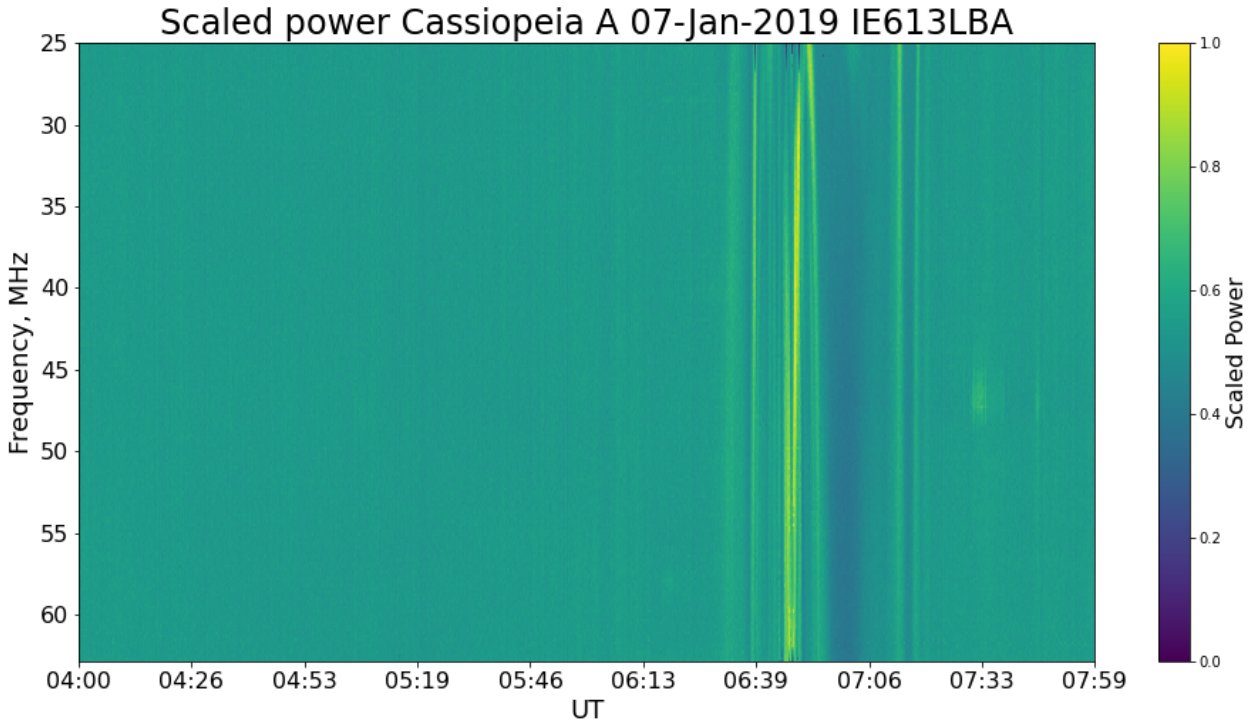
Scaled power Cassiopeia A 07-Jan-2019 IE613LBA
Frequency, MHz
25
30
35
40
45
50
55
60
04:00
04:26
04:53
05:19
05:46
06:13
06:39
07:06
07:33
07:59
UT
Scaled Power
0.0
0.2
0.4
0.6
0.8
1.0

2. Dynamic spectra from the Irish LOFAR station (IE613LBA) showing observations of Cygnus A (top panel) and Cassiopeia A (bottom panel).

In all cases where ionospheric features were observed, the ionosphere beforehand and afterward was undisturbed, enabling an unambiguous identification of the start and end times. The fact that the feature is not seen during the UK-CygA observations is interesting; nor was it seen in any of the other LOFAR stations taking part in the same observation. This will be discussed in the following section. Given that such high time resolution is available, some sections of the various features observed are shown in more detail in Figure 3.

With such closer examination, finer structures can be discerned within. At the lower frequencies some slight curvature in the vertical structures can be seen, particularly in Irl-CassA. Between the main vertical bright features in all dynamic spectra, fainter but similar vertical structures are visible within darker regions which, at lower resolution, might be regarded as signal fades, hinting at the cascade of turbulent scale sizes within the scattering plasma. In Irl-CygA some of the vertical features near the middle of the event can be seen to split into doublets in the higher frequency ranges of ~45-65 MHz.

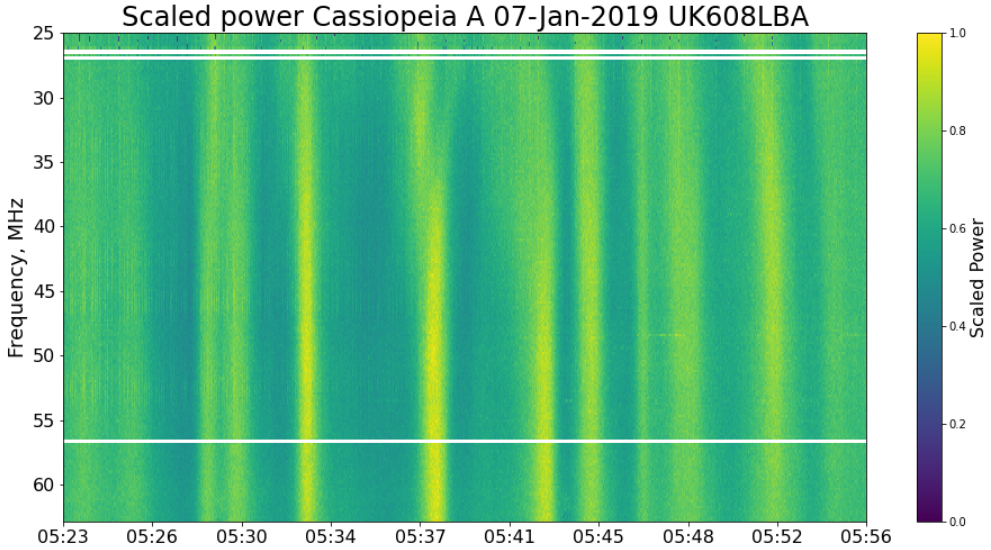
Scaled power Cassiopeia A 07-Jan-2019 UK608LBA
Frequency, MHz
25
30
35
40
45
50
55
60
05:23
05:26
05:30
05:34
05:37
05:41
05:45
05:48
05:52
05:56
Scaled Power
0.0
0.2
0.4
0.6
0.8
1.0

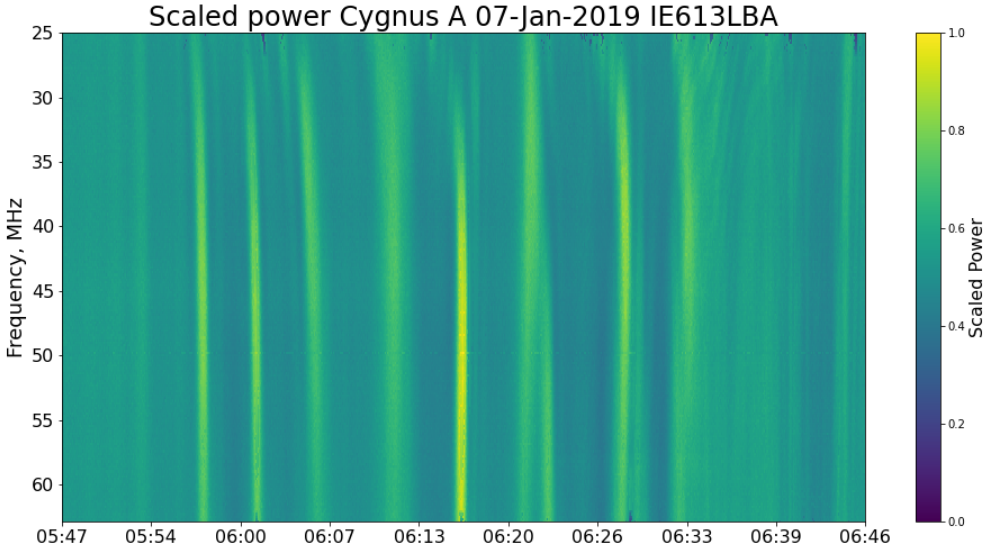
Scaled power Cygnus A 07-Jan-2019 IE613LBA
Frequency, MHz
25
30
35
40
45
50
55
60
05:47
05:54
06:00
06:07
06:13
06:20
06:26
06:33
06:39
06:46
Scaled Power
0.0
0.2
0.4
0.6
0.8
1.0

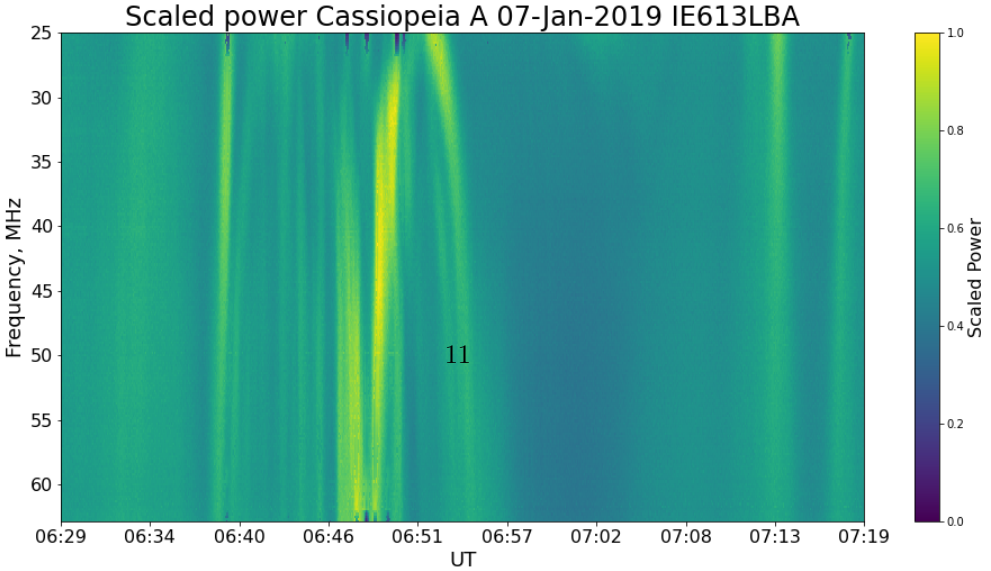
Scaled power Cassiopeia A 07-Jan-2019 IE613LBA
Frequency, MHz
25
30
35
40
45
50
55
60
06:29
06:34
06:40
06:46
06:51
06:57
07:02
07:08
07:13
07:19
UT
Scaled Power
0.0
0.2
0.4
0.6
0.8
1.0

Figure 3. Close up views of all features of interest in UKCassA, IrlCygA, and IrlCassA observations

3 Analysis

3.1 Geophysical Context

The Kp index at the start of the observations (0400) was 2+ and at the end (0800) had dropped slightly to 1+. Local K-indices from the observatories at Eskdalemuir (55.3°N, 3.2°W) and Lerwick (60.2°N, 1.1°W) did not go above 1+ during the observation. The Dst index decreased slightly from -5 to -15 nT over the course of the observing period. No solar radio bursts were recorded during the period of the event and the differences in event onset time at the different LOFAR stations demonstrate that these events were localised to the ionosphere rather than from emission sources in the solar wind. Figure 4 shows the SYM-H, ASY-H, and ASY-D indices from 0000-1200 UT on 7 January 2019; neither ASY-H nor ASY-D exceed +/- 25 nT during this time period. Geomagnetic conditions at this time were therefore quiet.

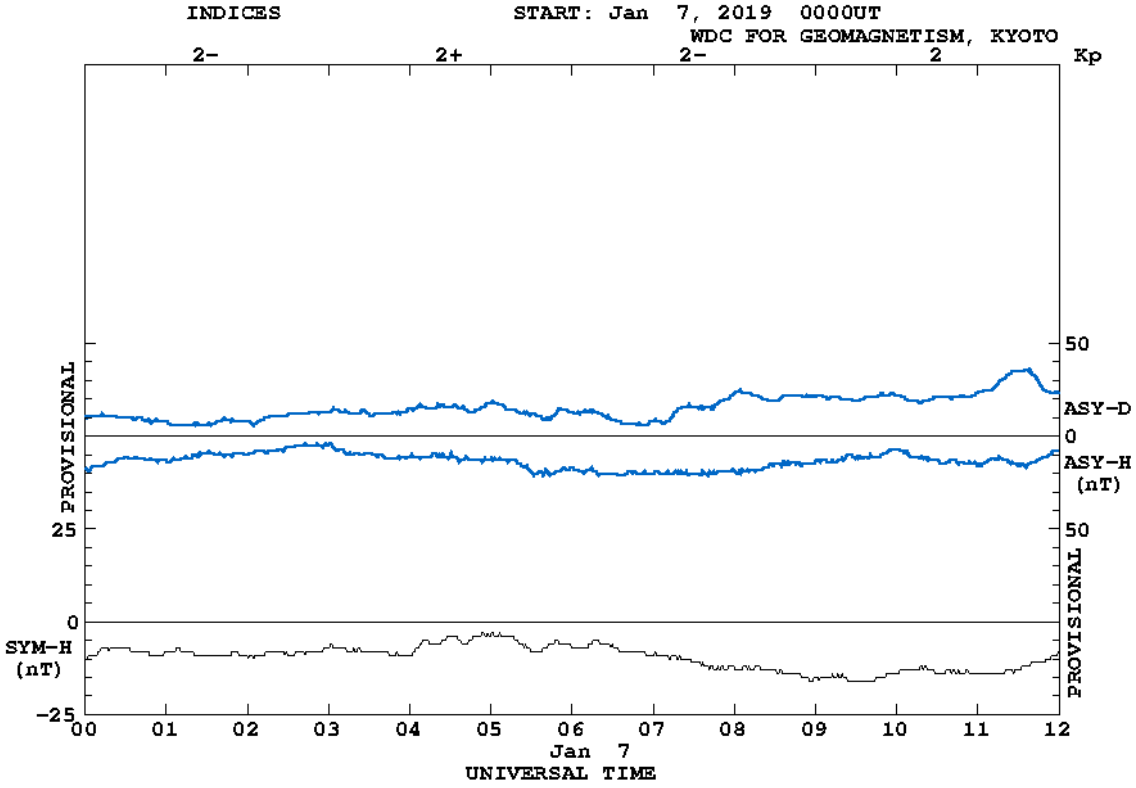

Figure 4. ASY-D, ASY-H, and SYM-H indices from 0000-1200 UT on 7 Jan 2019, showing quiet geomagnetic conditions.

3.2 GNSS TEC anomalies and ionosondes

To characterise the overall morphology and position of the feature seen in the LOFAR data and to further explain why the feature was not seen in UK-CygA, vertical Total Electron Content (vTEC) anomaly maps have been produced using data from ground based GNSS stations throughout the UK. The processing used to generate these maps is outlined in detail in Themens et al. (2022). These maps, seen in Figure 5, show relative deviations in vTEC from a running 30-minute averaged value of TEC. GNSS coverage is mostly constrained to the land area of the UK; however, these maps use data from GNSS satellites at all elevations >30°, enabling some coverage over the surrounding sea. Each pixel has a resolution of 0.5° in longitude and latitude. Ionospheric features are shown for an approximate projection altitude of 400 km. Yellow indicates a positive deviation in relative vTEC, blue shows a negative drop in relative vTEC.

A traveling ionospheric disturbance (TID), comprised of at least two clear positive TEC anomaly wave peaks (in yellow) and interspersed with negative TEC anomaly troughs (in blue), is clearly resolved over Southern England and is seen to propagate slowly from Southeast to Northwest from 0500-0600 (Figure 5, left panels). The wavelengths of the TID are approximately 3° at the resolution of the maps, corresponding to a distance of approximately 300 km. Indicative of the slow propagation of the TID is the fact that it is not seen in versions of these maps using a 7-minute running average (not shown).

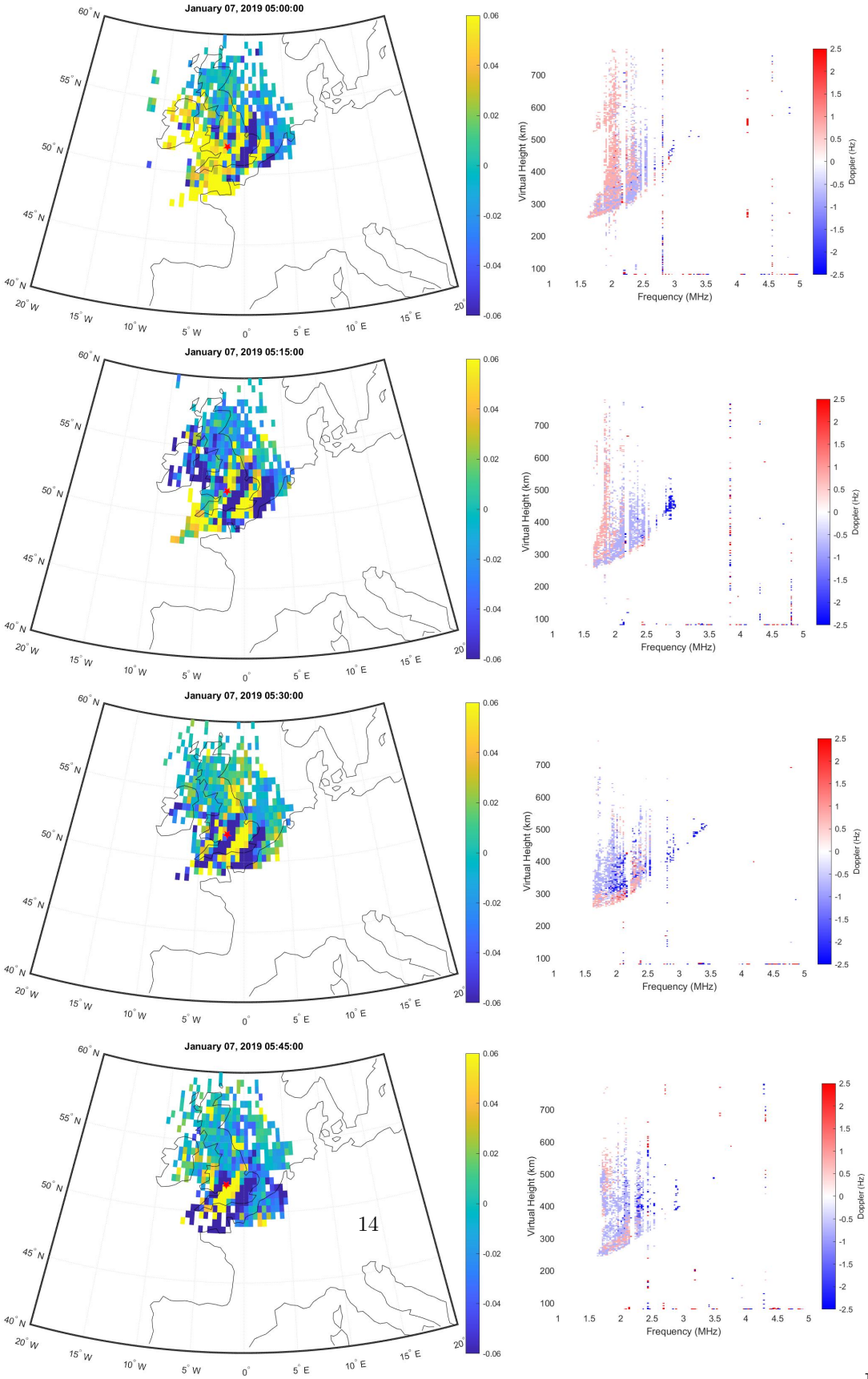
January 07, 2019 05:00:00
January 07, 2019 05:15:00
January 07, 2019 05:30:00
January 07, 2019 05:45:00
60° N
55° N
50° N
45° N
40° N
20° W
15° W
10° W
5° W
0°
5° E
10° E
15° E
20°
0.06
0.04
0.02
0
-0.02
-0.04
-0.06
Virtual Height (km)
Frequency (MHz)
Doppler (Hz)

Figure

5. GNSS TEC anomaly maps from 0500-0545 in 15-minute time steps, using 30-minute averaged GNSS data and time coincident Doppler ionograms from the Fairford ionosonde (position indicated by red star).

The position of the Fairford ionosonde (red star, Figure 5) underlies the propagation of the TID. Ionosondes emit radio waves in a vertical cone above them which backscatter off ionospheric plasma and return to the receiver. Thus any population of moving plasma within the cone will induce a Doppler shift in the received backscatter which can be combined with angle of arrival information to infer the approach and recession of different plasma populations in different directions. It is important to note that the recession and approach of plasma populations revealed by a Doppler ionogram may also be due to a vertical velocity component. Doppler ionograms therefore provide a coarse overview of whether density gradients in the bulk plasma flow above them is approaching, resulting in blue-shifted backscatter, or receding, resulting in red-shifted backscatter.

For the Fairford ionosonde, in addition to echo power and angle of arrival information, a coarse measurement of the echo Doppler is measured within the ionogram mode. This is generally used to help filter extraneous features from the ionograms. While this is very coarse and does not compare to purpose-built ionosonde drift modes, it can be used to at least infer whether structures are moving toward or away from the instrument. Alongside the TEC anomalies, Figure 5 also shows four time-coincident Doppler ionograms from the Fairford ionosonde, where only the O-mode echoes have been plotted.

Figure 6 shows the Doppler ionograms from FF051 at 15-minute timesteps from 0400-0545 and azimuth ionograms, for O-mode echoes, for the same times. This time window covered the transition of the TID as it passed overhead. Multiple colours in the azimuth plots reveal the presence of multiple populations of plasma density gradients in the transmission cone of the ionosonde at different azimuths.

In the first plot for example, at 0400, the light-red in the Doppler ionogram reveals a general recession of plasma at all frequencies, with the exception of a small population of blueshifted echoes at ~2 MHz. These lower frequency echoes correspond to a region of lower plasma density which clearly lies in the same position as the purple in the corresponding azimuthal ionogram showing that this lower plasma density population lies to the West (purple in the azimuthal plot).

Generally, from 0400-0500, the predominantly red points in the azimuthal ionograms across the full frequency space indicate the majority of echoes are from North of the ionosonde and are suggestive of a Northwards background plasma gradient overhead. The redshifted echoes corresponding to this Northwards background may also indicate a general vertical lifting of the ionosphere as the first of the peaks in the TID approaches. Smaller short lived populations of echoes at multiple frequencies and azimuths are also present throughout this period which may be caused by the passage of smaller scale ionospheric structures

overhead.

At 0500 a clear population of green echoes appear at lower frequencies indicating the presence of an ionospheric density depletion to the South of the ionosonde. From 0515 onwards the colours become less coherent, with echoes coming from many directions and hence, many different plasma structures. This also coincides with Doppler ionograms which show a mixture of red and blue indicating that echoes are being received from some plasma that is approaching the ionosonde whilst other structures are receding. Taken together this shows rapid fluctuations in ionospheric plasma density gradient above the ionosonde as the highly structure peak in the TEC anomaly passes overhead.

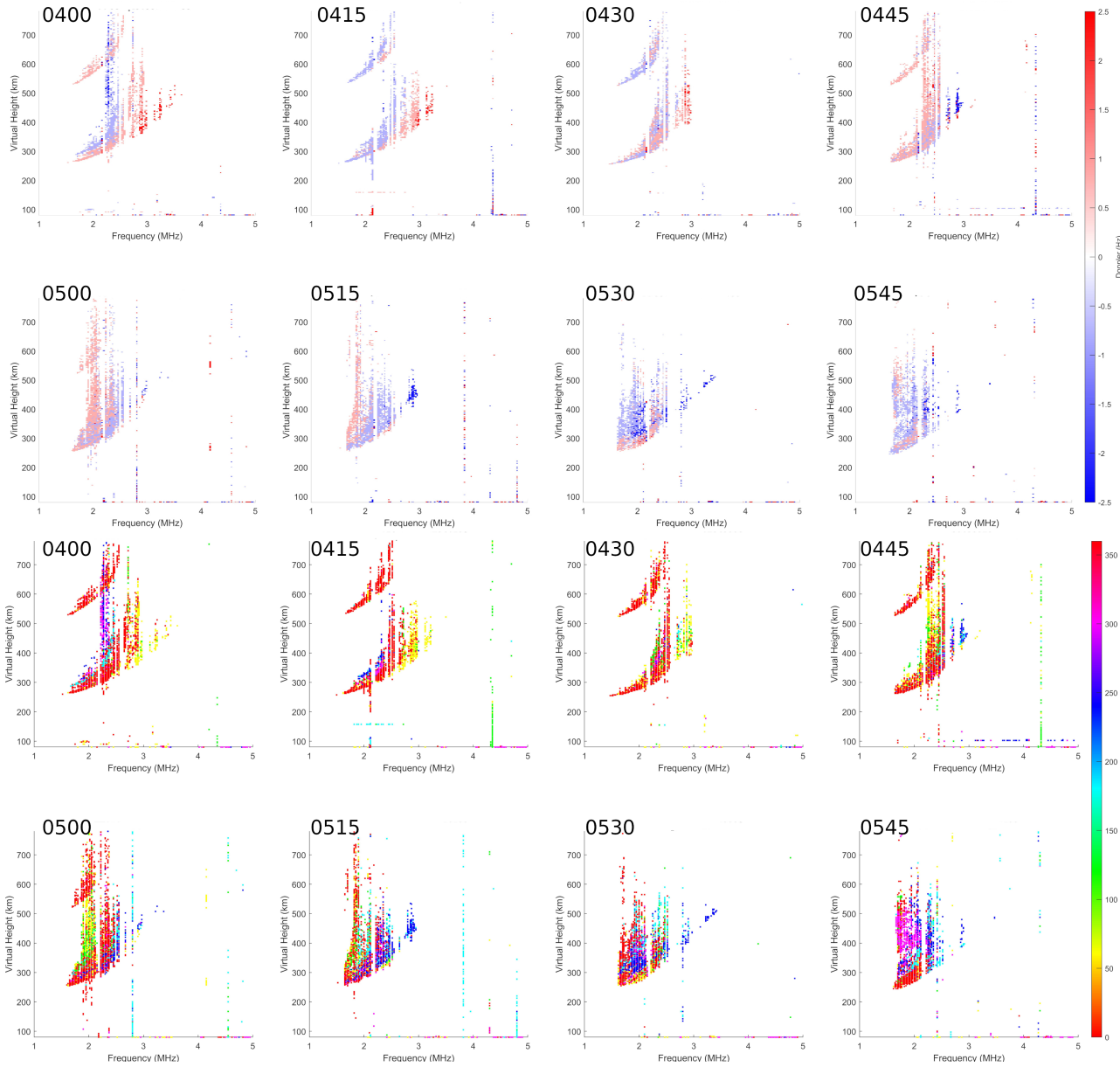

6. The upper 8 panels show Doppler ionograms every 15-minutes from 0400 to 0545 UT as the lead plasma enhancement of the TID passed over the Fairford ionosonde, followed by the approach of the plasma trough. Spread-F is also apparent throughout. The lower 8 panels show azimuthal ionograms from the same times.

From 0515-0545, significant populations of blue shifted plasma are seen in the Doppler plots, corresponding to azimuths to the Northwest. This corresponded

with the ionosonde lying beneath the trough of the TID; the peak was propagating away to the Northwest and as it moved out of the transmission cone the altitude of the bulk scattering plasma in the ionosphere decreased, causing blueshifting. A decrease in hmF2 from approximately 290 km to 260 km was seen during this period, as can be seen in the hmF2 plot in Figure 7.

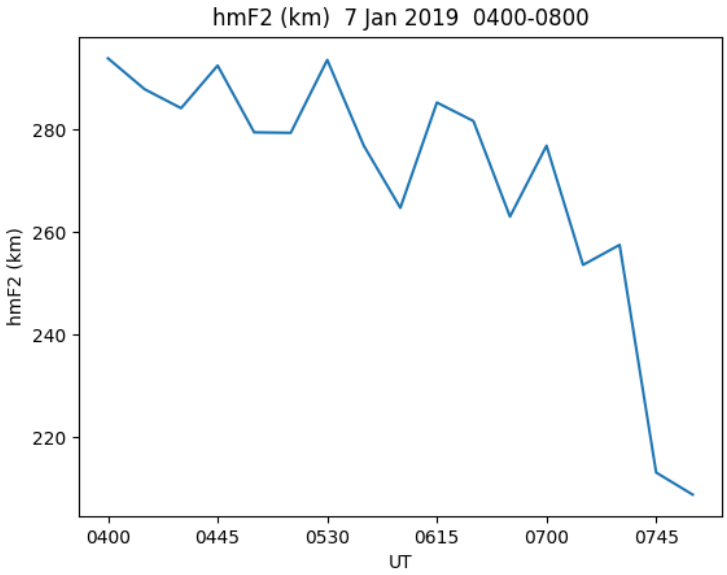

Figure 7. hmF2 from the Fairford ionosonde, 7-Jan-2019, 0400-0800 UT.

Moreover, the points on the later ionograms are more strongly clustered at lower plasma frequencies, which corresponds to a reduction in plasma density. These features are also consistent with the approach of the trough in the TID, between the first and second peaks. Clustering of the data points in all these ionograms is also consistent with spread-F and trace bifurcation, associated with TID presence in ionograms (Cervera and Harris, 2013; Moskaleva and Zaalov, 2013).

TIDs are compound structures which stretch over large height ranges, however these ionograms do enable a physical basis for the altitude of the TID to be estimated. As can be seen in Figure 7, the hmF2 altitude varied considerably over the course of the observing time between a maximum of 293 km and a minimum of 208 km, averaging at 270 km. This altitude was therefore used to constrain the LOFAR observing geometry shown in Section 3.3.

3.3 LOFAR observing geometry

Using the geometry outlined in Figure 1 of Birch et al., (2002), the angle subtended at the centre of the Earth ( ) between a line to the LOFAR station at ground level, of length R_E (radius of Earth), and another line extending to the ionospheric pierce point of length R_E+h, where h is the vertical height above

ground level that the IPP is situated, can be calculated as in (3).

$$\Psi = \cos^{-1}\left[\left(\frac{R_E}{R_E+h}\right)\cos\mathrm{E}\right] - E \quad (3)$$

where E is the elevation angle of the radio source as seen from the LOFAR station. The direct distance along the raypath from the LOFAR station to the IPP (L) can then be estimated, using a spherical Earth approximation, as shown in (4).

$$L = \sqrt{R_E^2 + (R_E+h)^2 - 2R_E(R_E+h)\cos\Psi} \quad (4)$$

Whilst it is not known exactly where in the raypath a given plasma feature is located, the altitude of the ionospheric pierce point (IPP) can be assumed based on data, such as ionogram virtual heights. The angle Ψ is also useful in another respect in that it can be used, again assuming a spherical Earth approximation, to calculate the Great Circle distance from the LOFAR station to a point on the Earth's surface directly beneath the IPP, as shown in (5).

$$d = 2\pi R_E\left(\frac{\Psi}{360}\right) \quad (5)$$

Once d is obtained, and given that we know the geographic location of the LOFAR station, the corresponding longitude and latitude on the Earth's surface directly beneath the IPP can be approximated using the inverse Haversine function. For a given initial longitude (lon_0) and latitude (lat_0) at the location of the LOFAR station, and the azimuth of the radio source (Az), the position (lon_1,lat_1) of the IPP can be calculated as in (6) and (7).

$$\mathrm{lat}_1 = \arcsin\left[\sin(\mathrm{lat}_0) * \cos\left(\frac{d}{R_E}\right) + \cos(\mathrm{lat}_0) * \sin\left(\frac{d}{R_E}\right) * \cos(\mathrm{Az})\right] \quad (6)$$

$$\mathrm{lon}_1 = \mathrm{lon}_0 + \mathrm{atan2}\left[\sin(\mathrm{Az}) * \sin\left(\frac{d}{R_E}\right) * \cos(\mathrm{lat}_1), \cos\left(\frac{d}{R_E}\right) - \sin(\mathrm{lat}_0) * \sin(\mathrm{lat}_1)\right] \quad (7)$$

Given that the elevation and azimuth of the radio source is obtainable from its RA and Declination, we can now calculate the location of the IPP for any given time in the observing window. The accuracy of this approach can be refined further with geodesic models that more precisely represent the shape of the Earth but, for our purposes, the current method is sufficient. Figure 8 shows the calculated IPP for the UK and Irish LOFAR stations of both radio sources for an IPP altitude of 270 km, based on the average hmF2 obtained from the Fairford ionosonde. The orange arc and blue arcs are positions of the IPP for Cassiopeia A, and Cygnus A, respectively throughout the observing window. The left hand pair of arcs are for the Irish LOFAR station, and the right hand pair are for the UK LOFAR station. The position and timing of event onsets in the various observations are also shown, as is the position of the LOFAR stations themselves, and other points of interest, such as the Fairford ionosonde, and ground based magnetometers at Lerwick (LER) and Eskdalemuir (ESK). The map is produced using the cartopy library routines in Python 3.

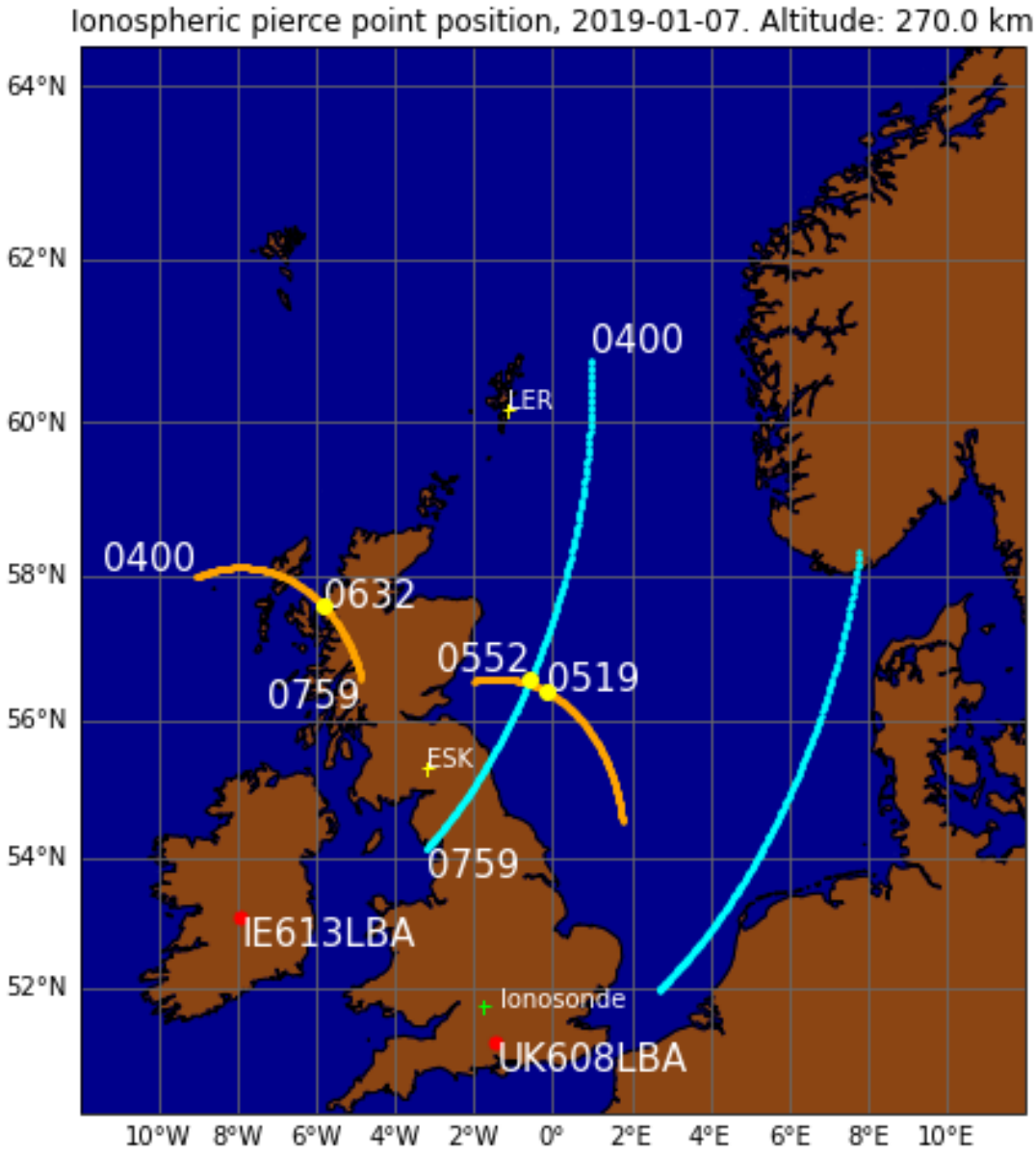

Figure 8. The positions of the IPP for the Irish and UK LOFAR stations observing Cassiopeia A (orange arcs) and Cygnus A (blue arcs). The timings and positions of the IPP at the beginning and end of the observing window, and the various event onset times are shown. The positions of the LOFAR stations, ionosondes, and the Lerwick (LER) and Eskdalemuir (ESK) magnetometers are also given. Note the absence of an event onset time/position in the Cygnus A arc for the UK LOFAR station as the event was not seen in this observation.

In Figure 8, for an assumed altitude of 270 km, the position of the IPP at event onset follows the time sequence of event onsets in the dynamic spectra (Figures 1 & 2). The feature is first seen, in any of the LOFAR data, at 0519 in UK-CassA. Onset is then seen at 0552 in Irl-CygA, and finally at 0632 in Irl-CassA. This would imply a TID propagating in an approximately West-North West direction, which is consistent with the GNSS TEC anomaly data shown in the previous section. The position of the UK-CygA IPP arc in Figure 8 (blue, far right) explains why no ionospheric scintillation from the TID was seen in the UK-CygA observations. For no plausible altitude does the UK-CygA arc lie far enough West to cross the position of the TID at any point, as seen in the GNSS TEC anomaly maps.

3.4 TID bulk structure and velocities

Initial velocity estimates can be calculated for the propagation of the TID by using the positions of the IPPs at the event onset times in each LOFAR observation, in combination with the great circle distance between them. These estimates are given in Table 2, and are based on the assumption that the events seen in UK-CassA, Irl-CygA, and Irl-CassA, are from the same ionospheric feature.

The positions of the IPPs and the movement of the TID in the GNSS TEC anomaly maps show that the TID was propagating approximately NorthWest. So first we establish a Cartesian co-ordinate system with a positive X-axis aligned West (270°) and positive Y-axis aligned North (0°) and express the TID propagation angle in terms of these coordinates rather than as the bearings shown in Table 2. By decomposing each of the velocity vectors into their X- (Westwards) and Y- (Northwards) components, and averaging, we find the TID was propagating at 63.6 ms^{-1}, on a bearing of 292.3°.

Transition	Bearing (°)	Distance (km)	Velocity (ms^{-1})
UKCassAonset > IrlCygA onset	307.6	26.2	16.2
UKCassAonset > IrlCassAonset	291.8	355.8	73.2
IrlCygA onset > IrlCassA onset	290.3	330.7	102.1

Table 2. Velocity estimates from event onset times. Transition column shows which two IPP positions are being used to estimate velocity. Bearing indicates initial bearing along great circle between the two positions.

The large scale topology and bulk flow characteristics of the TID are clearly seen in the relative vTEC maps and ionosonde data. As can be seen from the dynamic spectra (Figures 1 & 2), the lead wavefront contains sub-structure at much finer scale sizes with lifetimes in the raypath of a few minutes. Four frequency channels corresponding to 28.9, 36.7, 44.5, and 52.3 MHz in each of UK-CassA, Irl-CygA, and Irl-CassA, were used to calculate the power spectral density covering the time occupied by the events seen in each observation, and each of these are shown in Figure 9.

In each case the power spectra show a fairly typical appearance for ionospheric scintillation, namely a flat plateau at the lowest frequencies which rapidly steepens (at the Fresnel frequency, f_F) and descends to the noise floor. The region of lowest frequencies below the f_F are from received signal power that has not yet fully formed a scintillation pattern during travel from the ionosphere to the observer. The region enclosed between the Fresnel frequency and the steep descent to the noise floor is signal power from fully formed ionospheric scintillation. The power spikes seen in UK-CassA are caused by residual RFI (they are notably absent from the 28.9 MHz channel). Strong cross-frequency coherence can be observed in these spectra, particularly in the UK-CassA and Irl-CygA observations, with the same Fresnel frequency being seen in each. Irl-CassA is slightly less coherent, consistent with the more prominent curvature of features seen in the dynamic spectra from this observation (Figure 3, bottom panel).

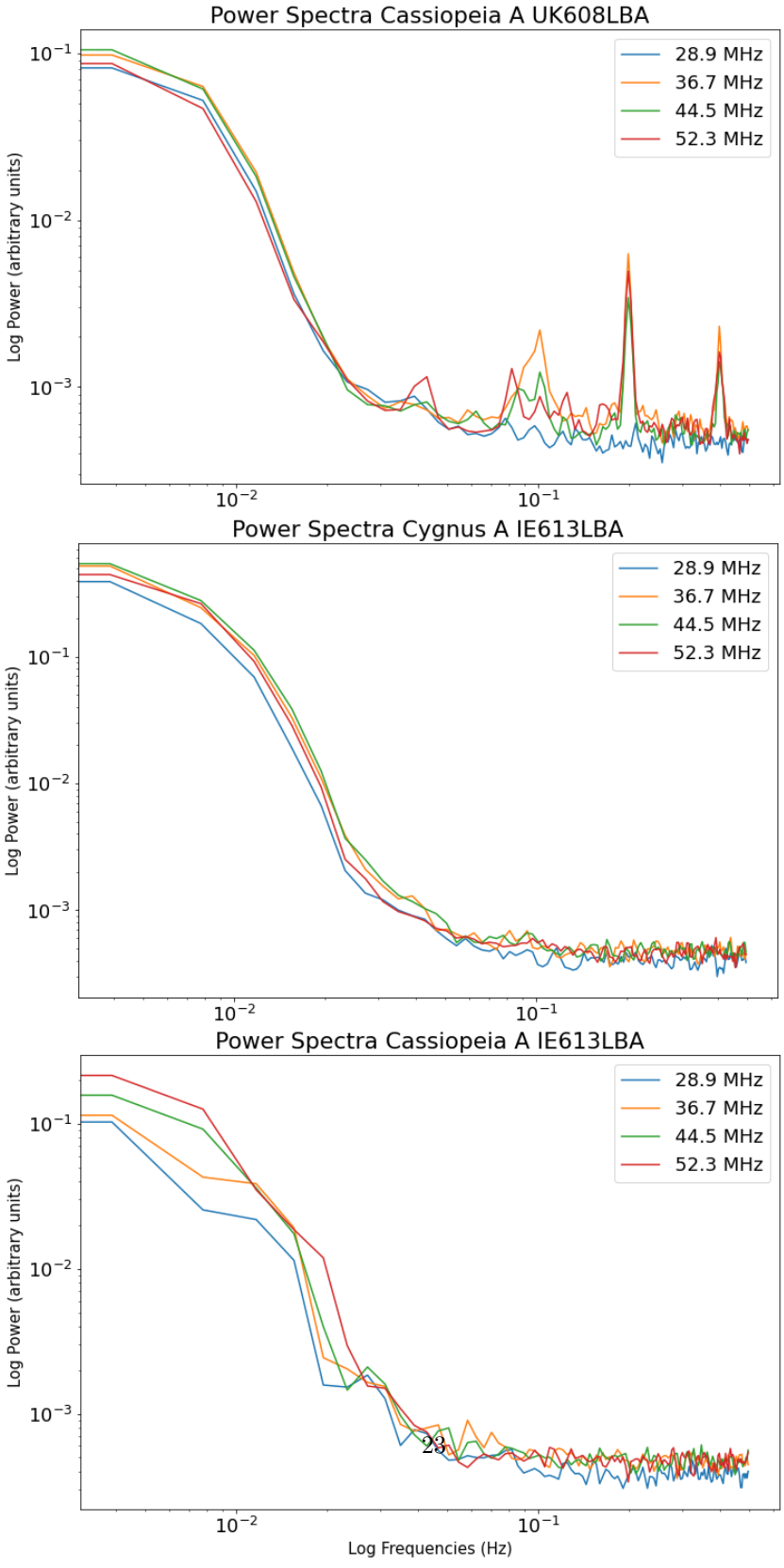
Power Spectra Cassiopeia A UK608LBA
28.9 MHz
36.7 MHz
44.5 MHz
52.3 MHz
Log Power (arbitrary units)
10^{-1}
10^{-2}
10^{-3}
10^{-2}
10^{-1}
Power Spectra Cygnus A IE613LBA
28.9 MHz
36.7 MHz
44.5 MHz
52.3 MHz
Log Power (arbitrary units)
10^{-1}
10^{-2}
10^{-3}
10^{-2}
10^{-1}
Power Spectra Cassiopeia A IE613LBA
28.9 MHz
36.7 MHz
44.5 MHz
52.3 MHz
Log Power (arbitrary units)
10^{-1}
10^{-2}
10^{-3}
10^{-2}
10^{-1}
Log Frequencies (Hz)

Figure

9. Power spectra for UK-CassA, Irl-CygA, and Irl-CassA at selected frequencies. The steepening of the spectra at 0.008 Hz is the Fresnel frequency.

By combining the Fresnel frequency information from the power spectra with the calculated Fresnel scale sizes at the midpoints of each event observed, using (1) and (4), we can estimate the plane-of-sky velocity of the plasma. The Fresnel scale, F_D, was calculated for the extrema of the bandwidth used by the LOFAR LBA, 25 MHz, and 65 MHz, and a middle frequency of 45 MHz. As the events recorded in the LOFAR data lasted for tens of minutes, the distance from the LOFAR station to the IPP at 270 km altitude, at the approximate midpoint of each event was used as the position of the event. The LOFAR-IPP distances (L) were calculated for UK-CassA, Irl-CygA, and Irl-CassA, as 667 km, 630 km, and 592 km respectively. Table 2 shows the Fresnel scale sizes for the stated frequencies at the distances quoted. Using (2) we can calculate the component of ionospheric plasma drift velocity perpendicular to the LOFAR raypath (plane-of-sky), and these are also shown in table 3.

As a further test of the consistency of these methods for finding the TID propagation velocity, the components of velocity perpendicular to the LOFAR raypaths are also shown in table 3. These values can be multiplied by a cos correction, where is the angle between the TID propagation velocity vector, as obtained from the vector averaging method, and the plane-of-sky velocity vector as seen from the LOFAR stations (at 90° to observing azimuth). As can be seen in table 3, the results obtained by doing this in all three LOFAR observations are in very close agreement with the TID velocity obtained by vector averaging. It is notable that the velocity and propagation for similar events crossing the raypaths for the LOFAR core stations would be much better constrained given the large number of velocity vectors and power spectra that would be available. A further study investigating just such an event is currently ongoing.

Freq. (MHz) / (m)	**F_D for UK-CassA (m)**	**F_D for Irl-CygA (m)**	**F_D for Irl-Cass**
25 / 12.0	4002	3889	3769
45 / 6.7	2983	2899	2809
65 / 4.6	2482	2412	2338
L, F_D, and velocity	**UK-CassA**	**Irl-CygA**	**Irl-CassA**
L (km)	667	630	592
f_F (Hz)	0.008	0.008	0.008
v_p (ms^{-1}) for = 12 m	32	31	30
v_p (ms^{-1}) for = 6.7 m	24	23	22
v_p (ms^{-1}) for = 4.6 m	20	19	19
v_p (ms^{-1}) perp. to LOFAR raypath	25.3	24.3	23.7
SD (v_p)	6.2	5.0	4.6
Azimuth - 90°	280.36	321.73	294.58
cos corrected velocity	62.2	55.4	63.6

Table 3. Fresnel scale (F_D) and corresponding perpendicular component of

plasma drift velocity, for the midpoint of each observation. The Fresnel frequency, distances from the LOFAR station to the IPP (L) at the midpoint of the events seen in UK-CassA, Irl-CygA, and Irl-CassA, are also shown. TID propagation as calculated from vector averaging between the positions of the IPP (at 270 km altitude) yields a velocity of 63.6 ms^{-1}, at a propagation direction of 292.3°.

By looking again at the TEC maps it is also possible to estimate the bulk velocity of the TID by noting how long it takes to move across the maps. Figure 10 shows TEC anomaly maps in time sequence starting at 0500 UT and stepping forward until 0655 UT (the approximate midpoint of the event seen in Irl-CassA). Also shown are the positions of the LOFAR IPPs at the midpoint of the respective events (red spots). Each pixel in these maps and in the supplementary video is 0.5° in longitude and latitude which, at the surface of the Earth at mid latitude corresponds to a distance ~111 km. The TID takes approximately 30-minutes to cover a two pixel distance, so a simple distance over time estimate yields a velocity of ~61 ms^{-1}, which is in very close agreement with the velocity calculated by the LOFAR IPP vector averaging method, and the cos corrected velocities obtained using the power spectra. The full sequence of the TID propagation can be seen in the supplementary video to this paper.

The first panel in Figure 10 shows the positions of the two wavepeaks and the intervening trough of the TID at 0500 UT. The first time it was seen in LOFAR was 0519 UT in UK-CassA; the IPP at the approximate midpoint of the event, at 0540 UT, lies just beyond the lateral extent of the TID which is visible in GNSS data, as shown by the red dot. The blank areas are where no GNSS data was available to establish a TEC anomaly, but one can imagine the continuation of the lateral wavefront outwards to the NorthEast and overlying the IPP at 0540 UT. It is noticeable that by this time also the lead wavepeak has, in the GNSS data at least, begun to break up, with the middle portion of the wave peak having disappeared. By the time of the midpoints of the later events, in Irl-CygA, and Irl-CassA respectively, the entire TID has become too incoherent to be seen in the GNSS TEC anomaly data. It is evident that whilst the TID may no longer be coherent enough to appear in the GNSS data at these later times, it is certainly still present in the LOFAR data.

Understanding the motion of this particular TID was complicated by the fact that, as is apparent in the accompanying video, the direction of motion was not strictly perpendicular to the wavefront. As the TID moves NorthWest it can be seen that the second wave peak gradually twists clockwise by a few degrees as it moves. Furthermore, the second wave peaks also appears to drift Westwards from approximately 0600 UT onwards. This Westward drift demonstrates that this complex movement is not merely a projection artefact, but a genuine separation and independent evolution of the two wave peaks which initially comprised the TID.

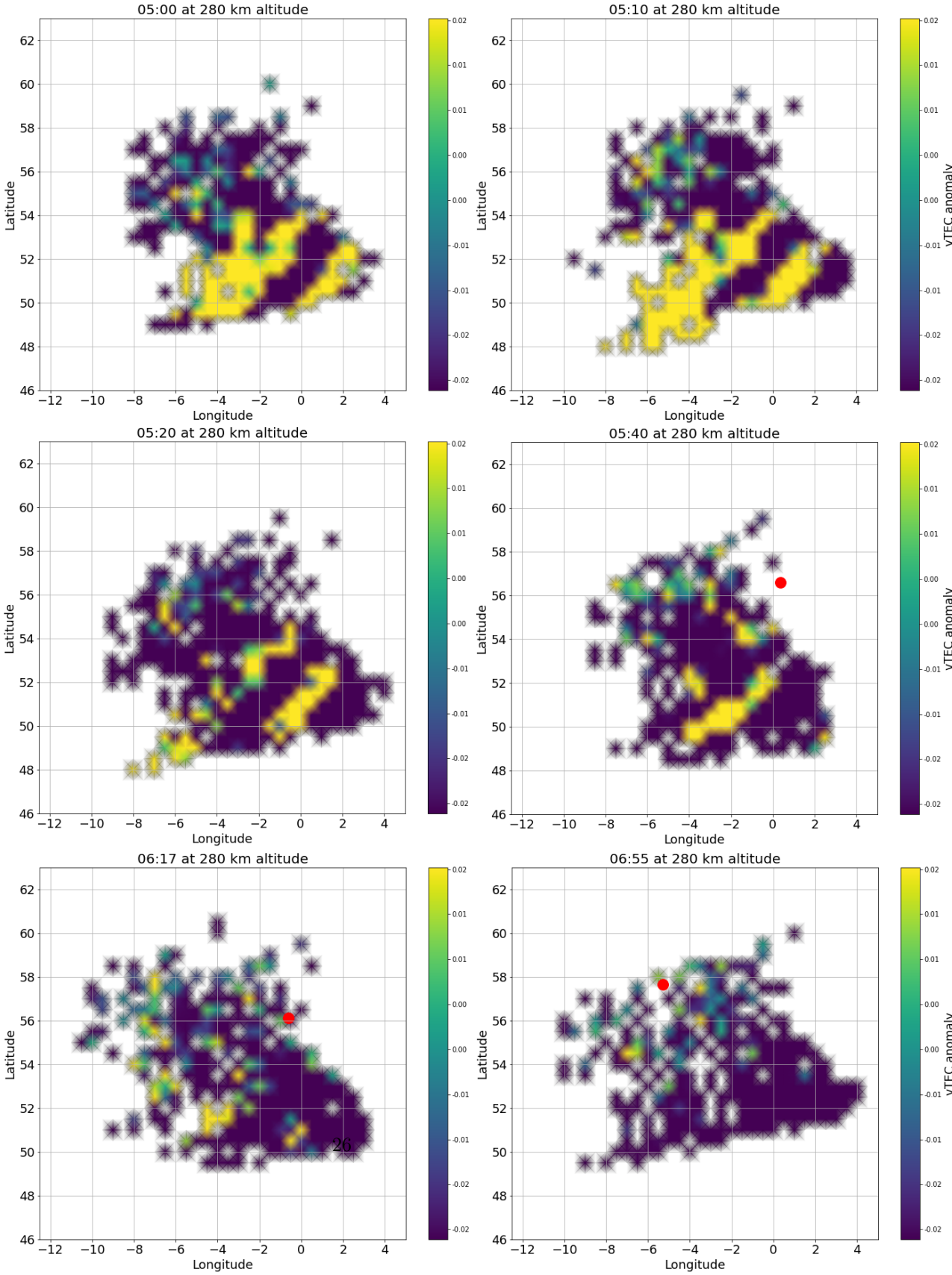
05:00 at 280 km altitude
05:10 at 280 km altitude
05:20 at 280 km altitude
05:40 at 280 km altitude
06:17 at 280 km altitude
06:55 at 280 km altitude
Latitude
Longitude
vTEC anomaly

10. GNSS TEC anomaly data, averaged to 30-minutes, showing the positions of the LOFAR IPPs (red spots) for the midpoints of the events in UK-CassA (0540 UT), Irl-CygA (0617 UT), and Irl-CassA (0655 UT) respectively. The TID position at 0500-0520 UT with both wavepeaks visible is also shown for context.

3.5 TID substructure

Having acquired several independent estimates for the bulk velocity of the TID it is possible to investigate the properties of the finer substructure lying within the TID itself as revealed by the LOFAR data (Figure 3). Given the slow speed of the TID and the length of time these substructures spend in the raypath they are likely to be quite large. One dimensional time series from the four representative frequencies of 28.9, 36.7, 44.5, and 52.3 MHz, as used in Section 3.4, but windowed to the time around the events, are shown in Figure 11.

From these time series one can clearly see that the dominant modes of oscillation in all three events, across all frequencies, are lasting for several minutes. In the data for Irl-CassA it can be seen that the TID has evolved significantly since it was seen earlier in Irl-CygA and UK-CassA, with a substantial signal fade lasting for approximately 20-minutes. Further, the signal enhancements taper to noticeably sharper peaks than the signal fades which are broader; this is particularly noticeable in UK-CassA and Irl-CygA.

Figure 12 shows averaged periodograms generated using Welch's method, using these representative frequencies, from all four observations. These periodograms include one for UK-CygA even though no event was seen in that one, hence it's flat appearance. This was performed simply as a control test. The other periodograms all show lifetimes of larger plasma features crossing the raypath of the order of 300-seconds. Given a plasma drift velocity of ~65 ms^{-1}, consistent with the velocity estimates in the previous section, the scale sizes of these features would be approximately 19.5 km. This is substantially larger than the Fresnel scale sizes calculated for the LOFAR wavelengths used here at LOFAR station-to-ionosphere distances of ~650 km (Table 3). Hence the dominant plasma sub-structures within the TID are generating refractive scattering, with smaller structure contributing some ionospheric scintillation to the total received signal.

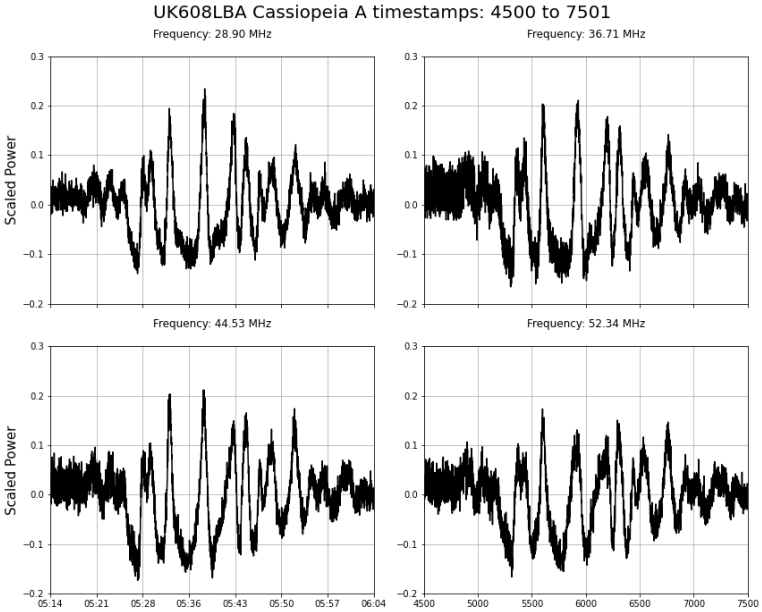
UK608LBA Cassiopeia A timestamps: 4500 to 7501
Frequency: 28.90 MHz
Frequency: 36.71 MHz
Frequency: 44.53 MHz
Frequency: 52.34 MHz
Scaled Power
05:14
05:21
05:28
05:36
05:43
05:50
05:57
06:04
4500
5000
5500
6000
6500
7000
7500

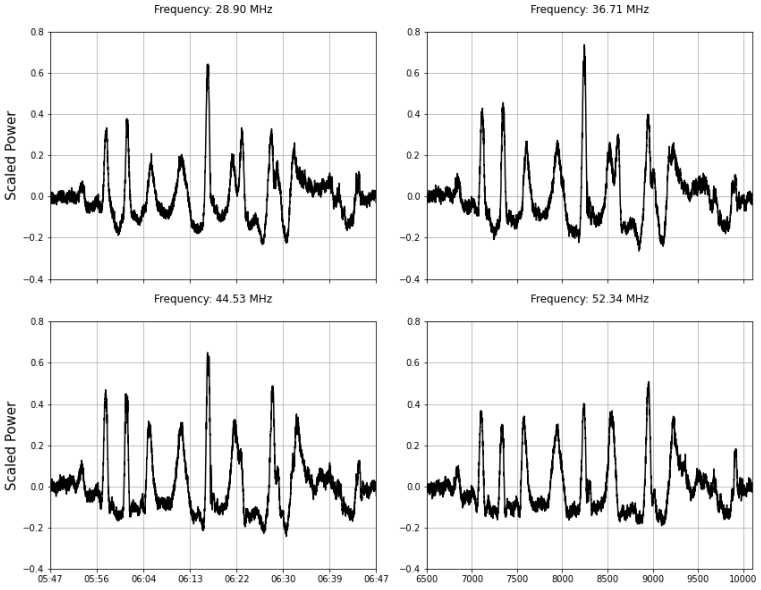
IE613LBA Cygnus A timestamps: 6500 to 10101
Frequency: 28.90 MHz
Frequency: 36.71 MHz
Frequency: 44.53 MHz
Frequency: 52.34 MHz
Scaled Power
05:47
05:56
06:04
06:13
06:22
06:30
06:39
06:47
6500
7000
7500
8000
8500
9000
9500
10000

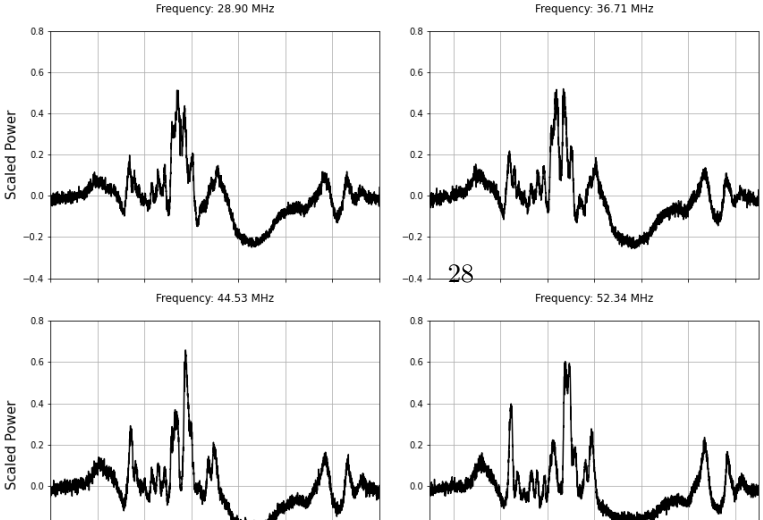
IE613LBA Cassiopeia A timestamps: 8750 to 12251
Frequency: 28.90 MHz
Frequency: 36.71 MHz
Frequency: 44.53 MHz
Frequency: 52.34 MHz
Scaled Power

One dimensional time series of LOFAR data for each event at the frequencies shown.

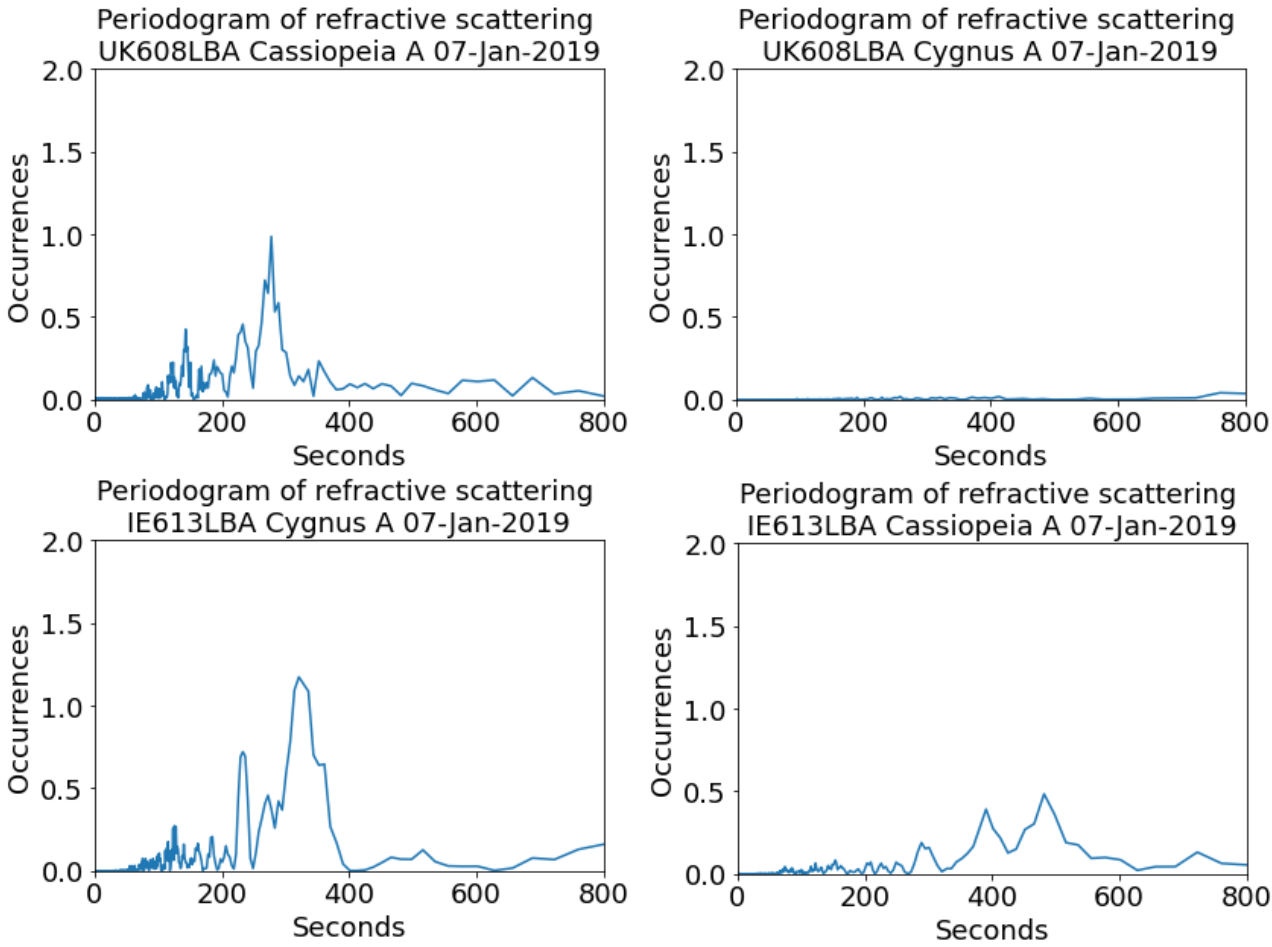

12. Periodograms generated using Welch's method, showing the dominant oscillation modes within the TID for UK and Irish LOFAR stations on Cygnus A and Cassiopeia A. The absence of any significant oscillations in the UK station observations for Cygnus A (top right) is consistent with the featureless dynamic spectrum for the same observation.

4. Discussion

The ionosphere in these observations is essentially behaving as a large and rapidly deformable lens. Signal enhancement features in the LOFAR data (Figure 11) tend to be shorter lived than signal fades and they tend to bracket fades. Others have explored the concept of natural ionospheric lensing in the past, such as Singleton (1970) and, more recently, Koval et al., (2017). A model is presently in development to investigate this concept with respect to LOFAR

observations in more detail, and will be published in an upcoming paper.

Fine structure signal enhancements can be exploited by radio astronomers by capturing the observing data at those points in time to produce, in principle, a higher resolution image of the target than would be possible if the ionosphere were not there. This is somewhat akin to the concept of lucky imaging in optical astronomy. Exploiting this effect across the entire LOFAR network would be very challenging given the localised scale sizes of the lensing features. However, given that each LOFAR station is in effect a radio telescope in its own right, this effect might still prove useful for radio astronomy observations from single stations. It may also be useful if exploited during observations from the LOFAR core, which contains many densely spaced individual LOFAR stations which would more likely all be under the same ionospheric fine structure if it is large enough.

Exploring substructure within TIDs has been attempted only a few times previously in the literature, such as by Alimov et al., (2008). These authors characterised the fractal nature of TIDs on spatial scales of ~1-10 km, quite closely matched to the size scales we have investigated here. Similarly, they made their observations at mid-latitude, under quiet geomagnetic conditions, by observing single frequency radio signals from orbital satellites at 150 MHz. TIDs are typically considered as compressional wave trains, with wavelengths extending sometimes for hundreds of km (e.g. Yang et al., 2017). However, results such as the present study, and Alimov et al., (2008), demonstrate that individual wave peaks within TIDs are themselves also comprised of wave trains on spatial scales smaller than the overall TID but larger than those which generate drifting ionospheric scintillation patterns from diffraction.

Overall, these observations demonstrate the usefulness of LOFAR as an ionospheric observatory and offer the possibility to understand ionosphere behaviour at previously unexplored time and frequency resolutions. The event described here was relatively simple and unambiguous; significantly more complex events are frequently encountered in the LOFAR archive, many showing highly-dispersive behaviour, which will require more thorough analysis in future work. Future work also entails developing an understanding of the relative importance of space weather versus terrestrial drivers of such phenomena.

5. Conclusions

We have investigated the characteristics of the propagation and fine substructure of a medium scale traveling ionospheric disturbance using wide bandwidth observations of trans ionospheric radio scattering with the LOFAR telescope. Further insights of the phenomena were obtained from ionosonde data and GNSS observations, which demonstrated it's approximate altitude, global morphology, and evolution. The TID was observed dissipating in GNSS TEC anomaly maps, whilst still being visible in LOFAR observations as a result of the different observing sensitivities involved. LOFAR observations revealed the presence of

refractive scattering from structures within the TID wave peak itself, with scale sizes of ~20 km, demonstrating LOFAR's utility as an ionospheric observatory.

Acknowledgements & Data Sources

This paper is based on data obtained with the International LOFAR Telescope (ILT) under project code LT10_006. LOFAR (van Haarlem et al. 2013) is the Low Frequency Array designed and constructed by ASTRON. It has observing, data processing, and data storage facilities in several countries, that are owned by various parties (each with their own funding sources), and that are collectively operated by the ILT foundation under a joint scientific policy. The ILT resources have benefitted from the following recent major funding sources: CNRS-INSU, Observatoire de Paris and Université d'Orléans, France; BMBF, MIWF-NRW, MPG, Germany; Science Foundation Ireland (SFI), Department of Business, Enterprise and Innovation (DBEI), Ireland; NWO, The Netherlands; The Science and Technology Facilities Council, UK; Ministry of Science and Higher Education, Poland. RAF was partially supported by the LOFAR4SW project, funded by the European Community's Horizon 2020 Programme H2020 INFRADEV-2017-1 under grant agreement 777442. The assistance of Chloe Ellerton with proof reading and technical checks is greatly appreciated. The LOFAR data used in this study are available from the LOFAR long-term archive: https://lta.lofar.eu/. The Kp- and Dst- indices are made available respectively by The Helmholtz Centre Potsdam-GFZ German Research Centre for Geosciences, and the World Data Centre for Geomagnetism, Kyoto. We thank the INTERMAGNET network, and ISGI (isgi.unistra.fr). The ACE solar wind data were sourced from the OMNI database at http://omniweb.gsfc.nasa.gov. This work at the University of Birmingham is supported by a research grant from the Leverhulme Trust. The services of the Natural Environment Research Council (NERC) British Isles continuous GNSS Facility (BIGF), www.bigf.ac.uk, in providing archived GNSS data to this study, are gratefully acknowledged. B. Dabrowski and A Krankowski thank the National Science Centre, Poland for granting "LOFAR observations of the solar corona during Parker Solar Probe perihelion passages" in the Beethoven Classic 3 funding initiative under project number 2018/31/G/ST9/01341. The UWM authors also thank the Ministry of Education and Science (MES), Poland for granting funds for the Polish contribution to the International LOFAR Telescope (agreement no. 2021/WK/02).

References

Aarons, J., (1982), Global morphology of ionospheric scintillations, Proceedings of the IEEE, vol. 70(4), pp. 360-378, doi: 10.1109/PROC.1982.12314

Abdu, M. A., Batista, I. S., Sobral, J. H. A., et al., (1985), Equatorial ionospheric plasma bubble irregularity occurrence and zonal velocity under quiet and disturbed conditions from Polarimeter observations, J. Geophys. Res., 90, 9921–9928, https://doi.org/10.1029/JA090iA10p09921, 1985.

Alimov, V.A., Vybornov, F.I. & Rakhlin, A.V., (2008), On the fractal structure of small-scale traveling ionospheric disturbances. *Radiophys Quantum El* **51,** 20–27. https://doi.org/10.1007/s11141-008-9001-2

Basu S, Weber E, Bullett T, Keskinen M, MacKenzie E, Doherty P, Sheehan R, Kuenzler H, Ning P, Bongiolatti J. (1998). Characteristics of plasma structuring in the cusp/cleft region at Svalbard. Radio Sci 33(6): 1885–1899. https://doi.org/10.1029/98RS01597.

Birch, M. J., Hargreaves, J. K., Bailey, G. J., (2002), On the use of an effective ionospheric height in electron content measurement by GPS reception, Radio Science, 37(1), doi:10.1029/2000RS002601

Booker, H. G., and Majidiahi, G., (1981), Theory of refractive scattering in scintillation phenomena, Journal of Atmospheric and Terrestrial Physics, 43(11), 1199-1214, doi:10.1016/0021-9169(81)90035-0.

Booker, H. G., (1981), Application of refractive scintillation theory to radio transmission through the ionosphere and the solar wind, and to reflection from a rough ocean, Journal of Atmospheric and Terrestrial Physics, 43(11),1215-1233, doi:10.1016/0021-9169(81)90036-2.

Bowman, G. G., (1981), The nature of ionospheric spread-F irregularities in midlatitude regions, Journal of Atmospheric and Terrestrial Physics, Vol. 43(1), pp. 65-79, ISSN 0021-9169, doi:10.1016/0021-9169(81)90010-6.

Briggs, B. H., Parkin, I. A. (1963), On the variation of radio star and satellite scintillations with zenith angle, J. Atmos. Terr. Phys. 25(6), 339-366.

Carrano, C. S., Groves, K. M., Caton, R. G., Rino, C. L., and Straus, P. R. (2011), Multiple phase screen modeling of ionospheric scintillation along radio occultation raypaths, *Radio Sci.*, 46, RS0D07, doi:10.1029/2010RS004591.

Cervera, M. A., and Harris, T. J. (2014), Modeling ionospheric disturbance features in quasi-vertically incident ionograms using 3-D magnetoionic ray tracing and atmospheric gravity waves, *J. Geophys. Res. Space Physics*, 119, 431– 440, doi:10.1002/2013JA019247.

Eltrass, A., Scales, W. A., Erickson, P. J., Ruohoniemi, J. M., and Baker, J. B. H. (2016), Investigation of the role of plasma wave cascading processes in the formation of midlatitude irregularities utilizing GPS and radar observations, *Radio Sci.*, 51, 836–851, doi:10.1002/2015RS005790.

Fallows, R. A., et al. (2014), Broadband meter-wavelength observations of ionospheric scintillation, *J. Geophys. Res. Space Physics*, 119, pages 10,544–10,560. doi:10.1002/2014JA020406.

Fallows, R. A., Bisi, M. M., Forte, B., et al., (2016), Separating nightside interplanetary and ionospheric scintillation with LOFAR, Astrophysical Journal Letters, 828(1), doi:10.3847/2041-8205/828/1/L7

Fallows, R. A., Forte, B., Astin, I., Allbrook, T., Arnold, A., Wood, A., Dorrian, G., Mevius, M., Rothkaehl, H., Matyjasiak, B., and 48 co-authors (2020), A LOFAR observation of ionospheric scintillation from two simultaneous travelling ionospheric disturbances, J. Space Weather Space Clim., 10, DOI: https://doi.org/10.1051/swsc/2020010

Fejer, B. G., Kelley, M. C., (1980), Ionospheric irregularities, Reviews of Geophysics and Space Physics, 18(2), 401-405.

Forte, B. (2008), Refractive scattering evidence from multifrequency scintillation spectra observed at auroral latitudes, *Radio Sci.*, 43, RS2012, doi:10.1029/2007RS003715.

Fremouw, E. J., Bates, H. F., (1971), Worldwide behaviour of average VHF/UHF scintillation, Radio Science, Vol. 6(10), pp 863-869. Confidential manuscript submitted to Geophysical Research Letters

van Haarlem, M. P., Wise M. W., Gunst, A. W., et al., (2013), LOFAR: Low-Frequency-Array, Astronomy & Astrophysics, 556(A2), doi:10.1051/0004-6361/201220873

Hinder, R., and Ryle, M., (1971), Atmospheric limitations to the angular resolution of aperture synthesis radio telescopes, MNRAS, 154, 229-253.

Galushko, V. G., Paznukhov, V. V., Yampolski, Y. M., et al., (1998), Incoherent scatter radar observations of AGW/TID events generated by the moving solar terminator, Annales Geophysicae, 16, 821-827.

de Gasperin, F., Mevius, M., Rafferty, D. A., et al., (2018), The effect of the ionosphere on ultra-low-frequency radio-interferometric observations, Astronomy & Astrophysics, 615, A179, doi:10.1051/0004-6361/201833012

Groves, K. M., Basu, S., Weber, E. J., et al., (1997), Equatorial scintillation and systems support, Radio Science, 32(5), 2047– 2064, doi:10.1029/97RS00836.

Kaplan, D., Tingay, S., Manoharan, P., et al. (2015), Murchison Widefield Array observations of anomalous variability: a serendipitous night-time detection of interplanetary scintillation, Astrophysical Journal Letters, 809, L12, doi:10.1088/2041-8205/809/1/L12

Karney, C. F. F., (2013), Algorithms for geodesics, Journal of Geodesics, 87:43–55 doi:10.1007/s00190-012-0578-z

Kinrade, J., Mitchell, C. N., Yin, P., et al., (2012), Ionospheric scintillation over Antarctica during the storm of 5–6 April 2010, J. Geophys. Res., 117, A05304, doi:10.1029/2011JA017073.

Kintner, P. M., Ledvina, B. M., de Paula, E. R. (2007), GPS and ionospheric scintillations, Space Weather, 5, S09003, doi:10.1029/2006SW000260.

Knepp, D. L., and Nickisch, L. J. (2009), Multiple phase screen calculation of wide bandwidth propagation, *Radio Sci.*, 44, RS0A09, doi:10.1029/2008RS004054.

Koval, A., Chen, Y., Stanislavsky, A., et al., (2017), Traveling ionospheric disturbances as huge natural lenses: Solar radio emission focusing effect, J. Geophys. Res. Space Physics, 122, 9092-9101, doi:10.1002/2017JA024080.

Little, C. G. (1951), A diffraction theory of the scintillation of stars on optical and radio wavelengths, Monthly Notices of the Royal Astronomical Society, Vol. 111, p. 289, doi:10.1093/mnras/111.3.289.Confidential manuscript submitted to Geophysical Research Letters

Mangum, J. G., and Wallace, P., (2015), Atmospheric Refractive Electromagnetic Wave Bending and Propagation Delay, Publications of the Astronomical Society of the Pacific, 127, 947, doi:10.1086/679582

Moskaleva, E. V., and Zaalov, N. Y. (2013), Signature of polar cap inhomogeneities in vertical sounding data, *Radio Sci.*, 48, 547– 563, doi:10.1002/rds.20060.

Mitchell, C. N., Alfonsi, L., De Franceschi, G., et al. (2005), GPS TEC and scintillation measurements from the polar ionosphere during the October 2003 storm, Geophysical Research Letters, 32, L12S03, doi:10.1029/2004GL021644.

Muralikrishna, P., Vieira, L. P., Abdu, M. A., (2007), Spectral features of E- and F-region plasma irregularities as observed by rocket-borne electron density probes from Brazil. Rev. Bras. Geof., vol. 25(2), pp.115-128.

Prikryl, P., Jayachandran, P. T., Chadwick, R, et al., (2015), Climatology of GPS phase scintillation at northern high latitudes for the period 2008 to 2013, Annales Geophysicae, vol. 33, pp.531-545, doi:10.5194/angeo-33-531-2015

Priyadarshi, S., (2015), A Review of Ionospheric Scintillation Models, Surv. Geophys. 36: 295. https://doi.org/10.1007/s10712-015-9319-1

Reinisch, B.W., Galkin, I.A. Global Ionospheric Radio Observatory (GIRO) (2011), *Earth Planet Sp.* **63,** 377–381. https://doi.org/10.5047/eps.2011.03.001

Singleton, D. G., (1970), Saturation and focusing effects in radio-star and satellite scintillations, *Journal of Atmospheric and Terrestrial Physics,* **32**, 187-208, https://doi.org/10.1016/0021-9169(70)90191-1.

K. Song, K. Meziane, A. Kashcheyev and P. T. Jayachandran, (2022), "Multifrequency Observation of High Latitude Scintillation: A Comparison With the Phase Screen Model", *IEEE Transactions on Geoscience and Remote Sensing*, vol. 60, pp. 1-9, 2022, Art no. 5801209, doi: 10.1109/TGRS.2021.3113778.

Stone, E. C., Fransden, A. M., Mewaldt, R. A., et al. (1998), The Advanced Composition Explorer, Vol. 86(1-4), Space Science Reviews, pp. 1-22, doi: 10.1023/A:1005082526237

Themens, D. R., Watson, C., Žagar, N., Vasylkevych, S., Elvidge, S., McCaffrey, A., et al. (2022). Global propagation of ionospheric disturbances associated with the 2022 Tonga volcanic eruption. *Geophysical Research Letters*, 49, e2022GL098158. https://doi.org/10.1029/2022GL098158

Tsunoda, R. T. (1985), Control of the seasonal and longitudinal occurrence of equatorial scintillations by the longitudinal gradient in integrated E region Pedersen conductivity, Journal of Geophysical Research, 90(A1), 447-456, doi:10.1029/JA090iA01p00447.

Tsunoda, R. T. (1988). High latitude F-region irregularities: A review and synthesis. Reviews of Geophysics, 26, 719.

RamaRao, P. V. S., TulasiRam, S., Gopi Krishna, S., et al., (2006), Morphological and spectral characteristics of L-band and VHF scintillations and their impact on trans-ionospheric communications, Earth Planet Space Science, 58, 895-904

Rishbeth, H., Setty, C. S. G. K., (1961), The F-layer at sunrise, Journal of Atmospheric and Terrestrial Physics, Vol. 20(4), pp. 263-276, doi:10.1016/0021-9169(61)90205-7.Confidential manuscript submitted to Geophysical Research Letters

Wild, J. P., Roberts, J.A. (1956), The spectrum of radio-star scintillations and the nature of irregularities in the ionosphere, Journal of Atmospheric and Terrestrial Physics, Volume 8, Issues 1–2, Pages 55-75, https://doi.org/10.1016/0021-9169(56)90091-5.

Yang, H., E. Monte-Moreno, andM. Hernández-Pajares (2017), Multi-TID detection and characterization in a dense Global NavigationSatellite System receiver network, *Journal Geophysical Research: Space Physics*, 122, 9554–9575, doi:10.1002/2017JA023988

Yeh, K. C., Liu, C.-H. (1982), Radio wave scintillations in the ionosphere, Proceedings of the IEEE, vol. 70, p. 324-360.

Observation	Cassiopeia A Elevation	Cassiopeia A Azimuth	Cygnus A Elevation	Cygnus A Azimuth	Notes
UK608LBA					
	°	°	°	°	Observation Start
	°	°	Event not seen	Event not seen	Event onset, Cass. A
	°	°	Event not seen	Event not seen	Event end, Cass. A
	°	°	°	°	Observation End
IE613 LBA					
	°	°	°	°	Observation Start

			°	°	Event onset, Cyg. A
	°	°			Event onset, Cass. A
			°	°	Event end, Cyg. A
	°	°			Event end, Cass. A
	°	°	°	°	Observation End

Table 1. Observation summary and approximate event timings from LOFAR observations of Cassiopeia A and Cygnus A on 7 January 2019.

Transition	Bearing (°)	Distance (km)	Velocity (ms^{-1})
UKCassAonset > IrlCygA onset	307.6	26.2	16.2
UKCassAonset > IrlCassAonset	291.8	355.8	73.2
IrlCygA onset > IrlCassA onset	290.3	330.7	102.1

Table 2. Velocity estimates from event onset times. Transition column shows which two IPP positions are being used to estimate velocity. Bearing indicates initial bearing along great circle between the two positions.

Freq. (MHz) / (m)	**F_D for UK-CassA (m)**	**F_D for Irl-CygA (m)**	**F_D for Irl-Cass**
25 / 12.0	4002	3889	3769
45 / 6.7	2983	2899	2809
65 / 4.6	2482	2412	2338
L, F_D, and velocity	**UK-CassA**	**Irl-CygA**	**Irl-CassA**
L (km)	667	630	592
f_F (Hz)	0.008	0.008	0.008
v_p (ms^{-1}) for = 12 m	32	31	30
v_p (ms^{-1}) for = 6.7 m	24	23	22
v_p (ms^{-1}) for = 4.6 m	20	19	19
v_p (ms^{-1}) perp. to LOFAR raypath	25.3	24.3	23.7
SD (v_p)	6.2	5.0	4.6
Azimuth - 90°	280.36	321.73	294.58
cos corrected velocity	62.2	55.4	63.6

Table 3. Fresnel scale (F_D) and corresponding perpendicular component of plasma drift velocity, for the midpoint of each observation. The Fresnel fre-

quency, distances from the LOFAR station to the IPP (L) at the midpoint of the events seen in UK-CassA, Irl-CygA, and Irl-CassA, are also shown. TID propagation as calculated from vector averaging between the positions of the IPP (at 270 km altitude) yields a velocity of 63.6 ms^{-1}, at a propagation direction of 292.3°.

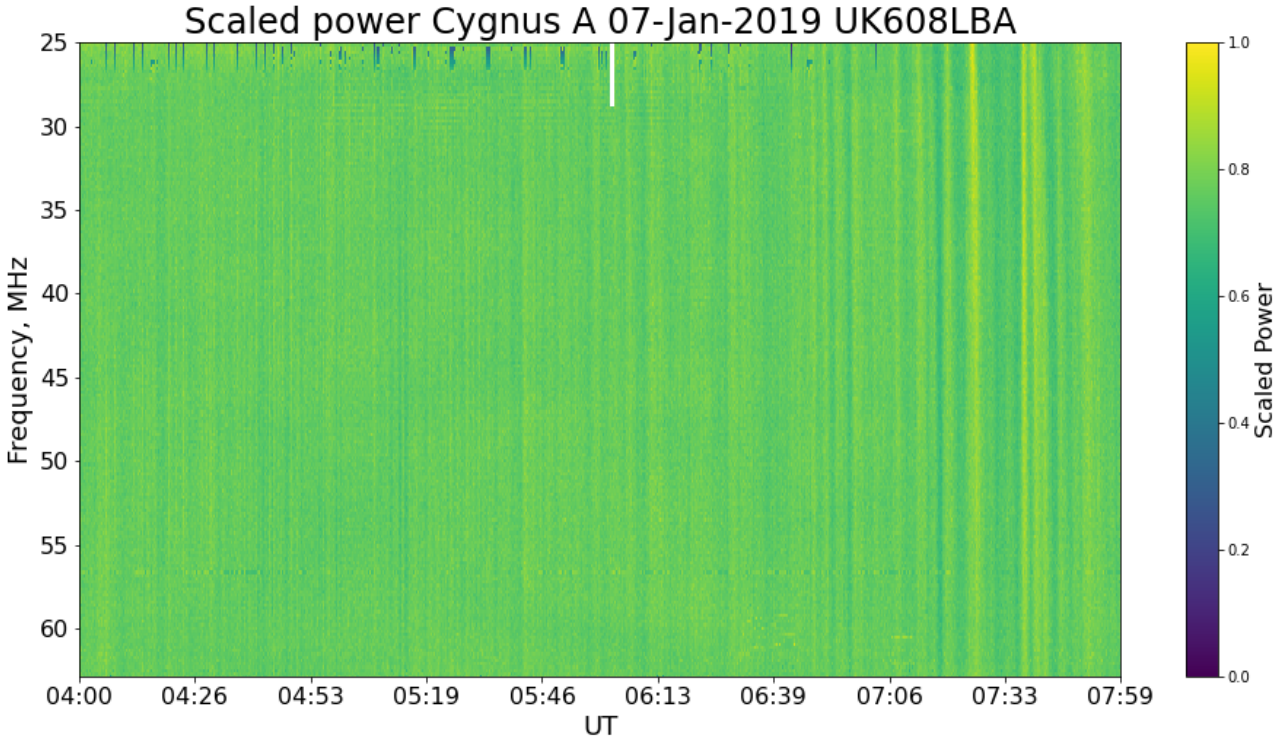
Scaled power Cygnus A 07-Jan-2019 UK608LBA
Frequency, MHz
25
30
35
40
45
50
55
60
04:00
04:26
04:53
05:19
05:46
06:13
06:39
07:06
07:33
07:59
UT
Scaled Power
0.0
0.2
0.4
0.6
0.8
1.0

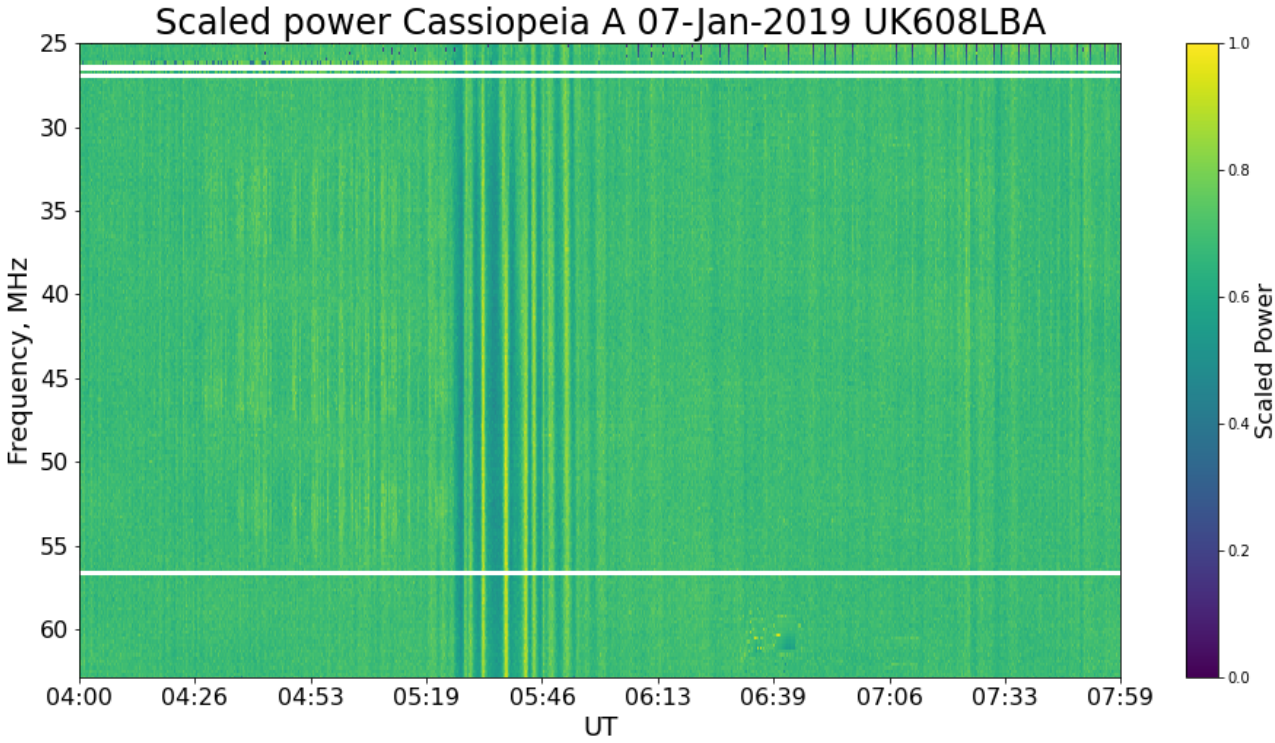
Scaled power Cassiopeia A 07-Jan-2019 UK608LBA
Frequency, MHz
25
30
35
40
45
50
55
60
04:00
04:26
04:53
05:19
05:46
06:13
06:39
07:06
07:33
07:59
UT
Scaled Power
0.0
0.2
0.4
0.6
0.8
1.0

1

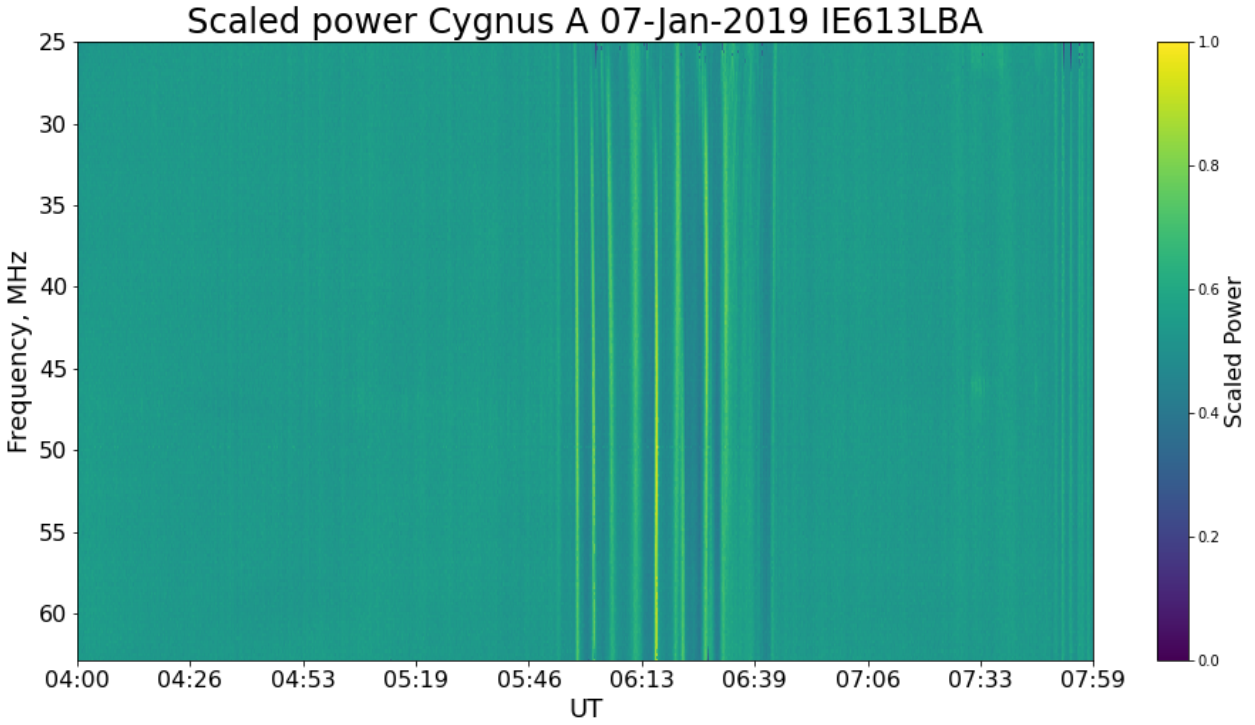
Scaled power Cygnus A 07-Jan-2019 IE613LBA
Frequency, MHz
25
30
35
40
45
50
55
60
04:00
04:26
04:53
05:19
05:46
06:13
06:39
07:06
07:33
07:59
UT
Scaled Power
0.0
0.2
0.4
0.6
0.8
1.0

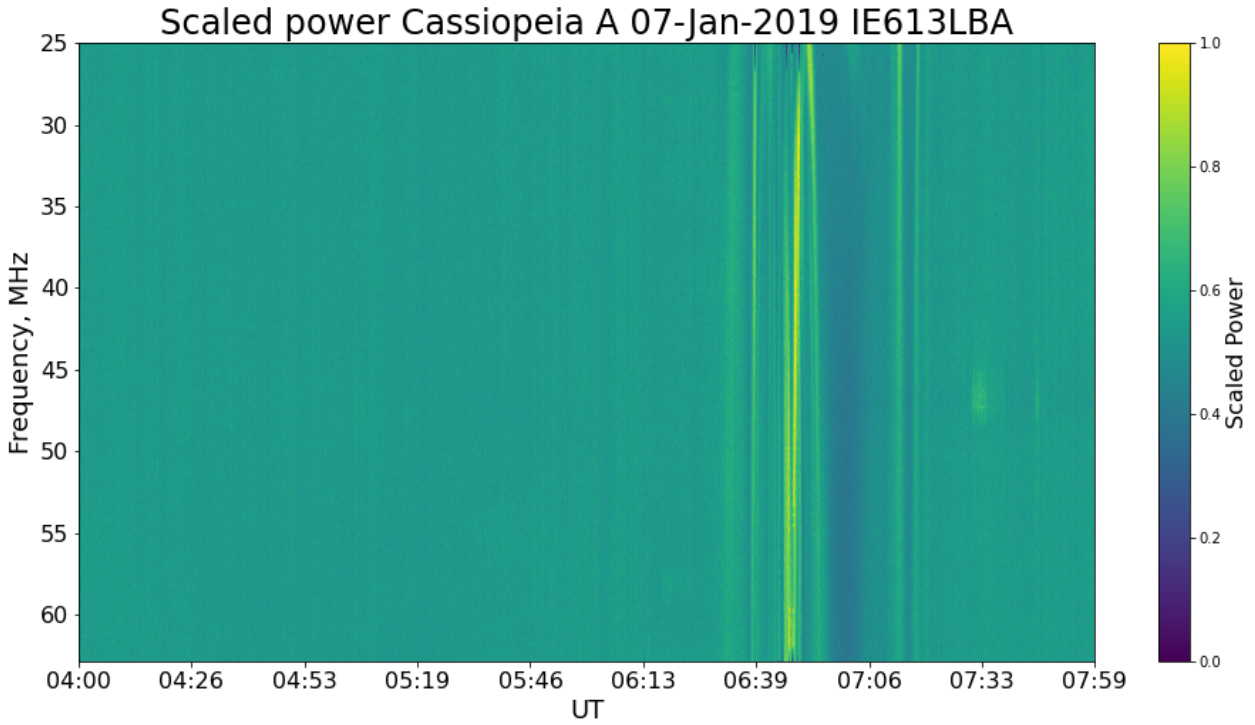
Scaled power Cassiopeia A 07-Jan-2019 IE613LBA
Frequency, MHz
25
30
35
40
45
50
55
60
04:00
04:26
04:53
05:19
05:46
06:13
06:39
07:06
07:33
07:59
UT
Scaled Power
0.0
0.2
0.4
0.6
0.8
1.0

2

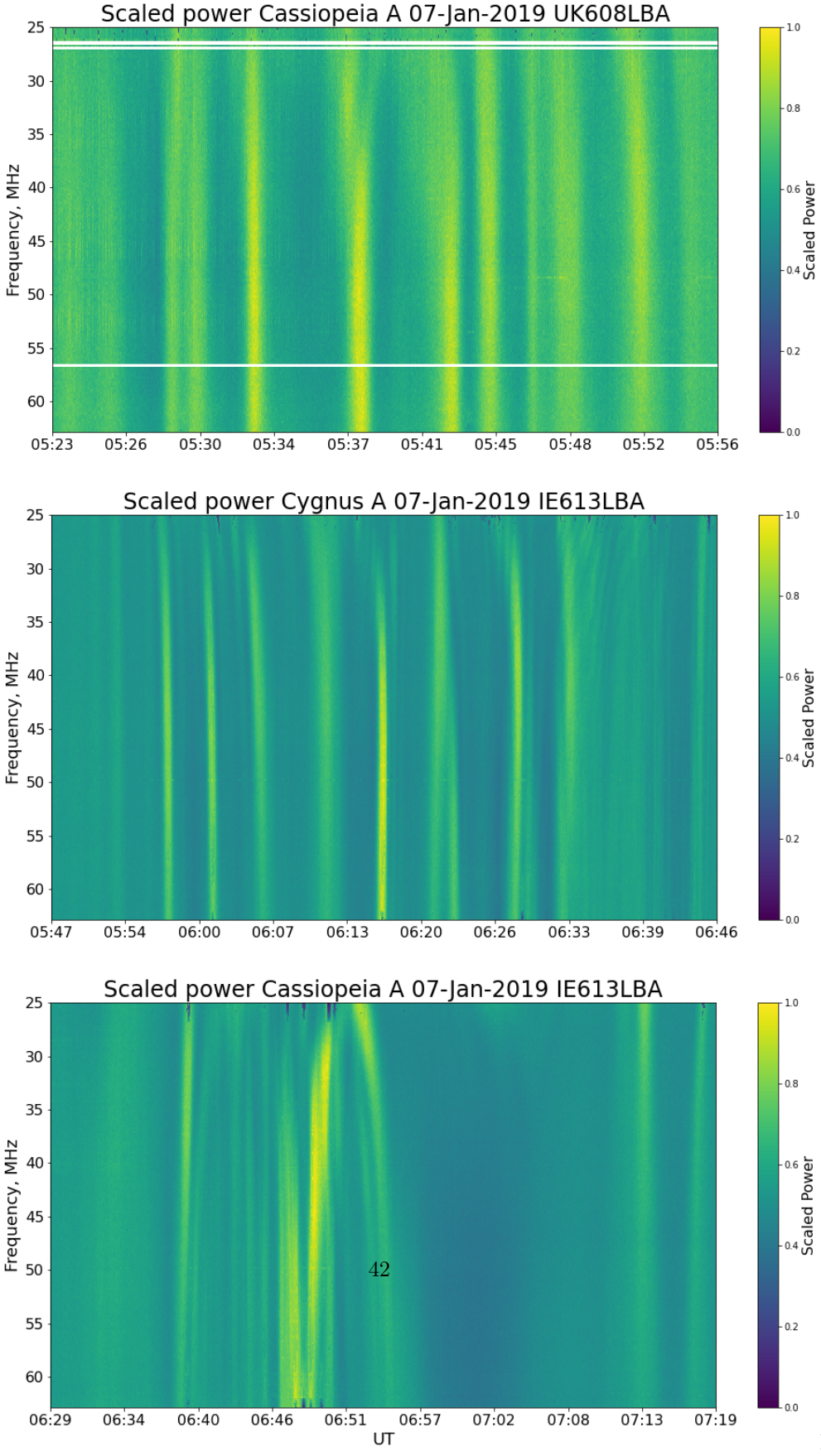
Scaled power Cassiopeia A 07-Jan-2019 UK608LBA
Frequency, MHz
25
30
35
40
45
50
55
60
05:23
05:26
05:30
05:34
05:37
05:41
05:45
05:48
05:52
05:56
Scaled Power
0.0
0.2
0.4
0.6
0.8
1.0
Scaled power Cygnus A 07-Jan-2019 IE613LBA
Frequency, MHz
05:47
05:54
06:00
06:07
06:13
06:20
06:26
06:33
06:39
06:46
Scaled Power
Scaled power Cassiopeia A 07-Jan-2019 IE613LBA
Frequency, MHz
06:29
06:34
06:40
06:46
06:51
06:57
07:02
07:08
07:13
07:19
UT
Scaled Power

Figure

3

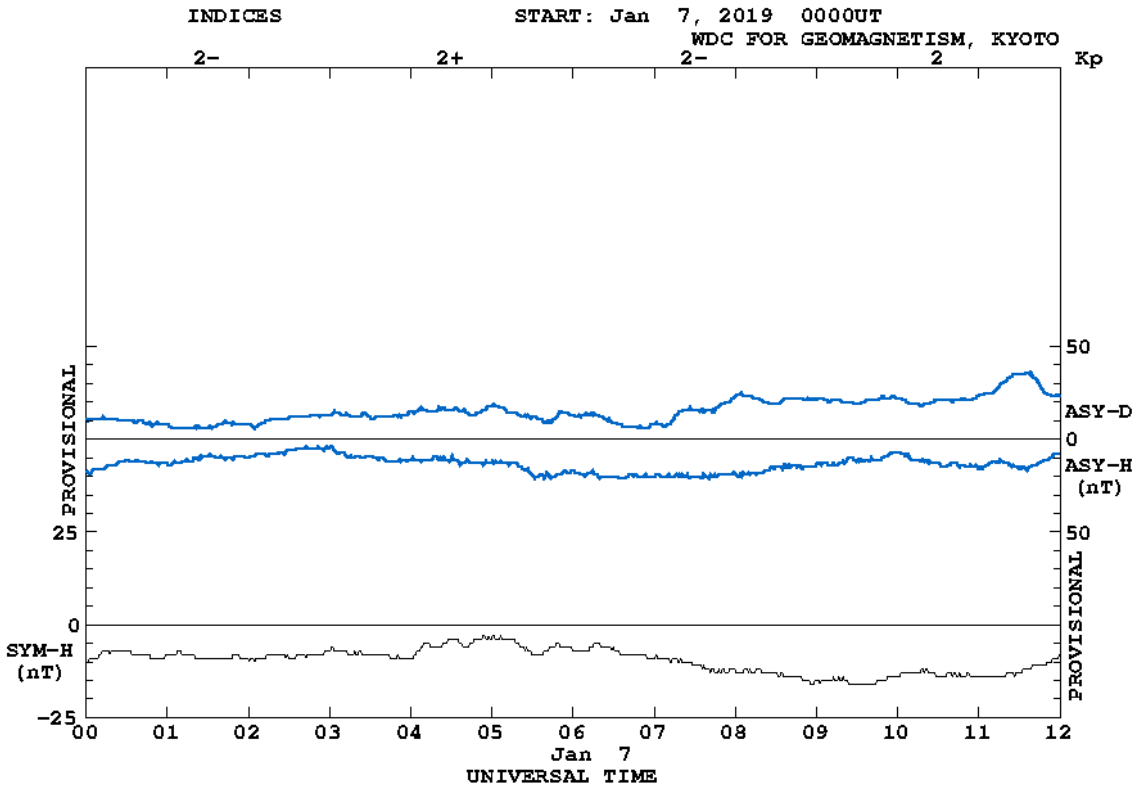
INDICES
START: Jan 7, 2019 0000UT
WDC FOR GEOMAGNETISM, KYOTO
2-
2+
2-
2
Kp
50
ASY-D
0
ASY-H
(nT)
50
PROVISIONAL
25
0
SYM-H
(nT)
-25
PROVISIONAL
00
01
02
03
04
05
06
07
08
09
10
11
12
Jan 7
UNIVERSAL TIME

Figure

4

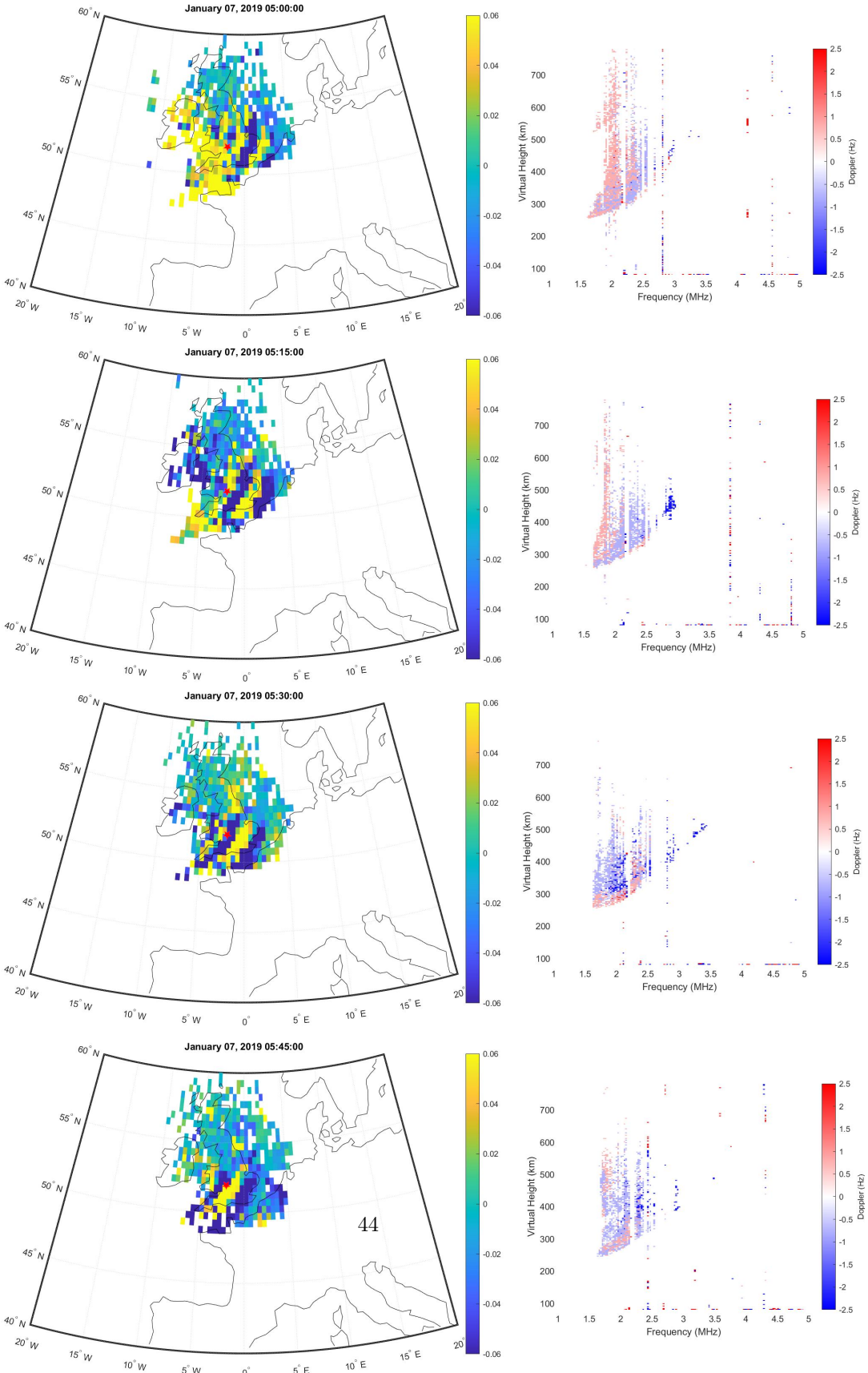
January 07, 2019 05:00:00
January 07, 2019 05:15:00
January 07, 2019 05:30:00
January 07, 2019 05:45:00
60° N
55° N
50° N
45° N
40° N
20° W
15° W
10° W
5° W
0°
5° E
10° E
15° E
20°
0.06
0.04
0.02
0
-0.02
-0.04
-0.06
Virtual Height (km)
Frequency (MHz)
Doppler (Hz)

Figure

5

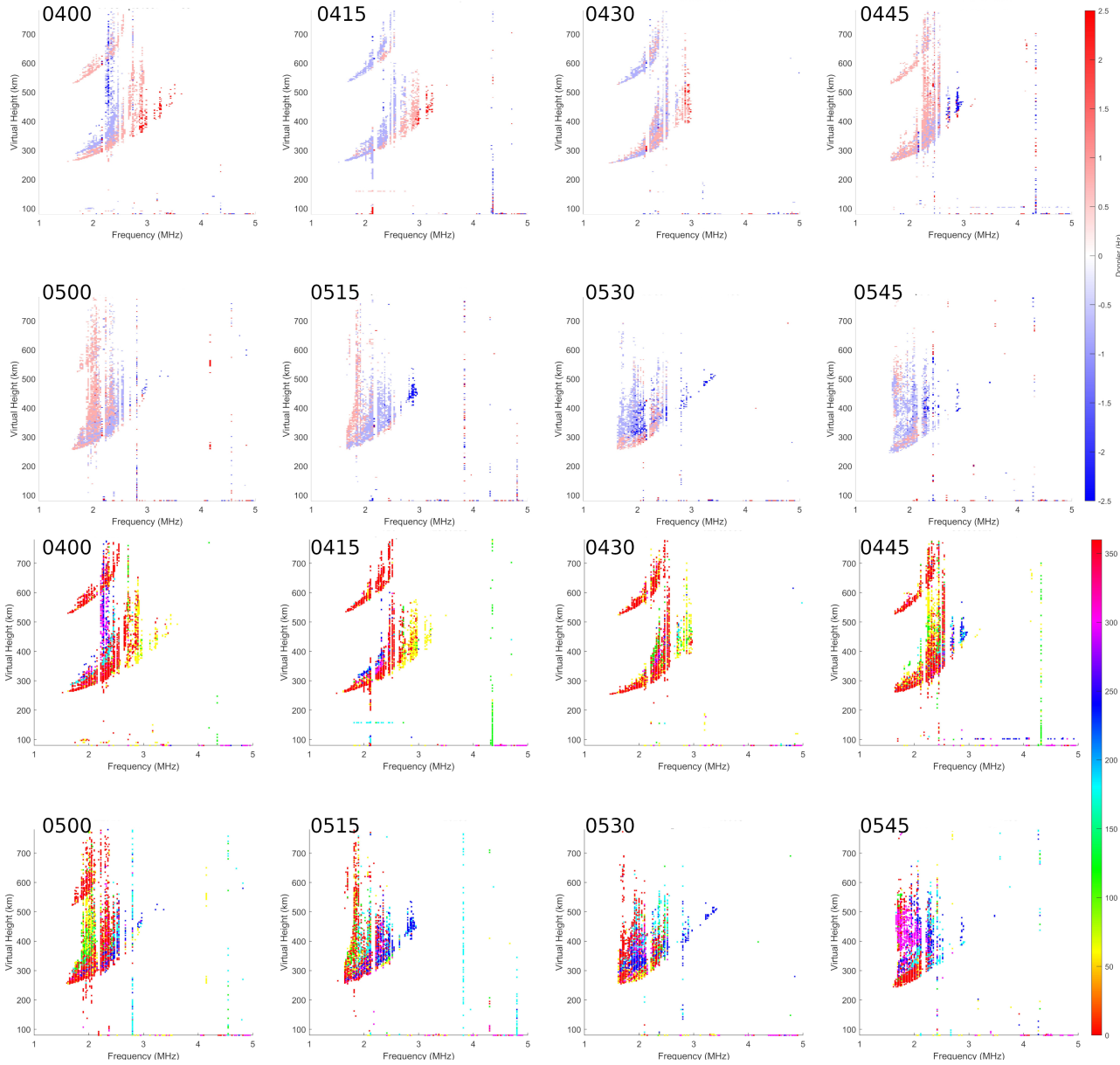
0400
0415
0430
0445
0500
0515
0530
0545
Virtual Height (km)
Frequency (MHz)
Doppler (Hz)

6

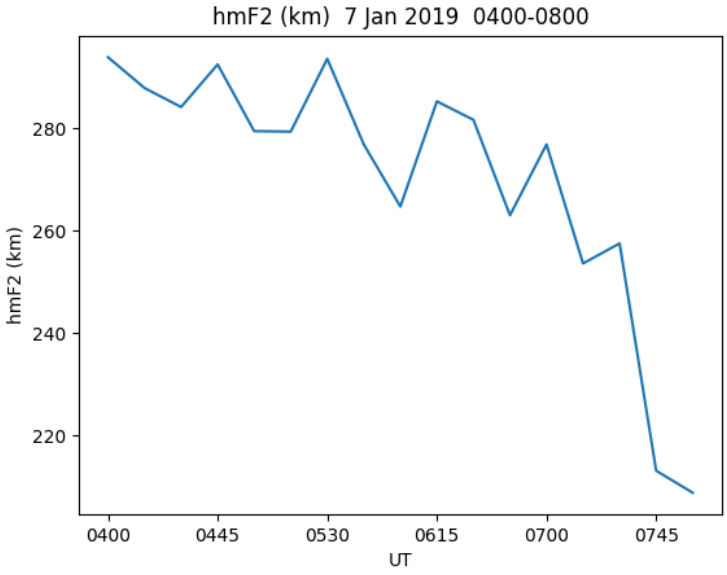
hmF2 (km) 7 Jan 2019 0400-0800
hmF2 (km)
280
260
240
220
0400
0445
0530
0615
0700
0745
UT

Figure 7

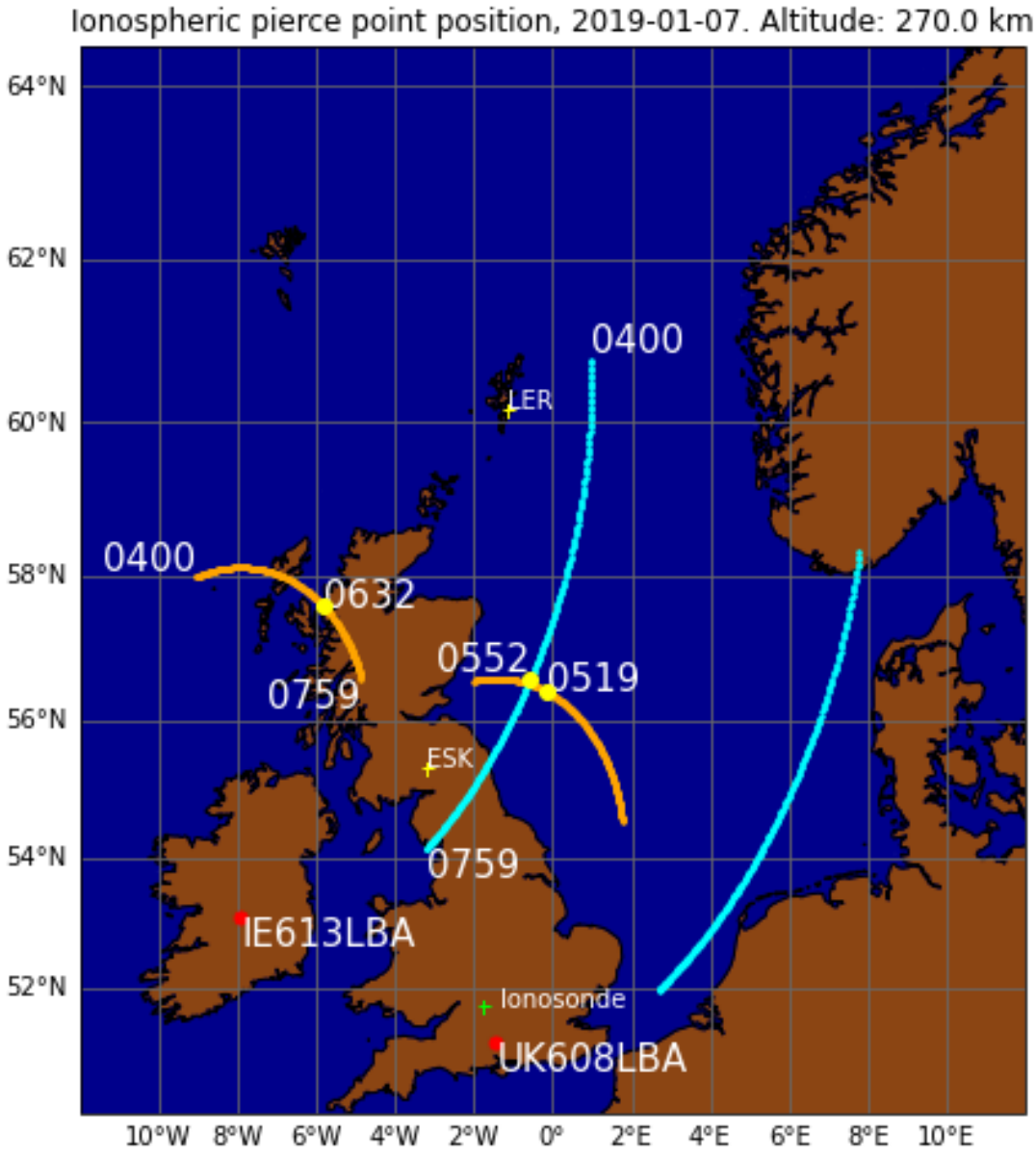
Ionospheric pierce point position, 2019-01-07. Altitude: 270.0 km
64°N
62°N
60°N
58°N
56°N
54°N
52°N
10°W
8°W
6°W
4°W
2°W
0°
2°E
4°E
6°E
8°E
10°E
0400
LER
0400
0632
0759
0552
0519
ESK
0759
IE613LBA
Ionosonde
UK608LBA

Figure 8

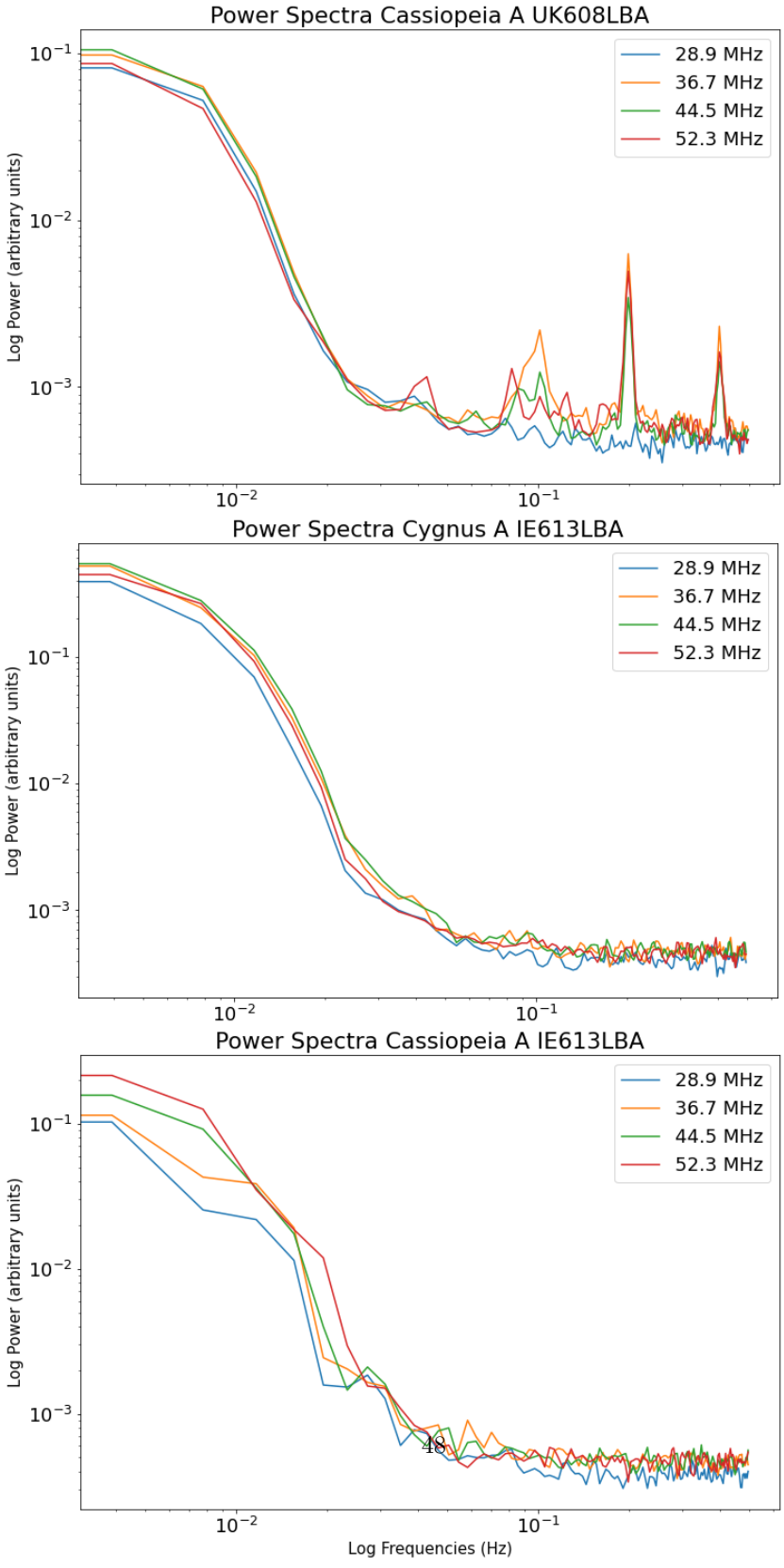
Power Spectra Cassiopeia A UK608LBA
28.9 MHz
36.7 MHz
44.5 MHz
52.3 MHz
Log Power (arbitrary units)
Power Spectra Cygnus A IE613LBA
Power Spectra Cassiopeia A IE613LBA
Log Frequencies (Hz)

Figure

9

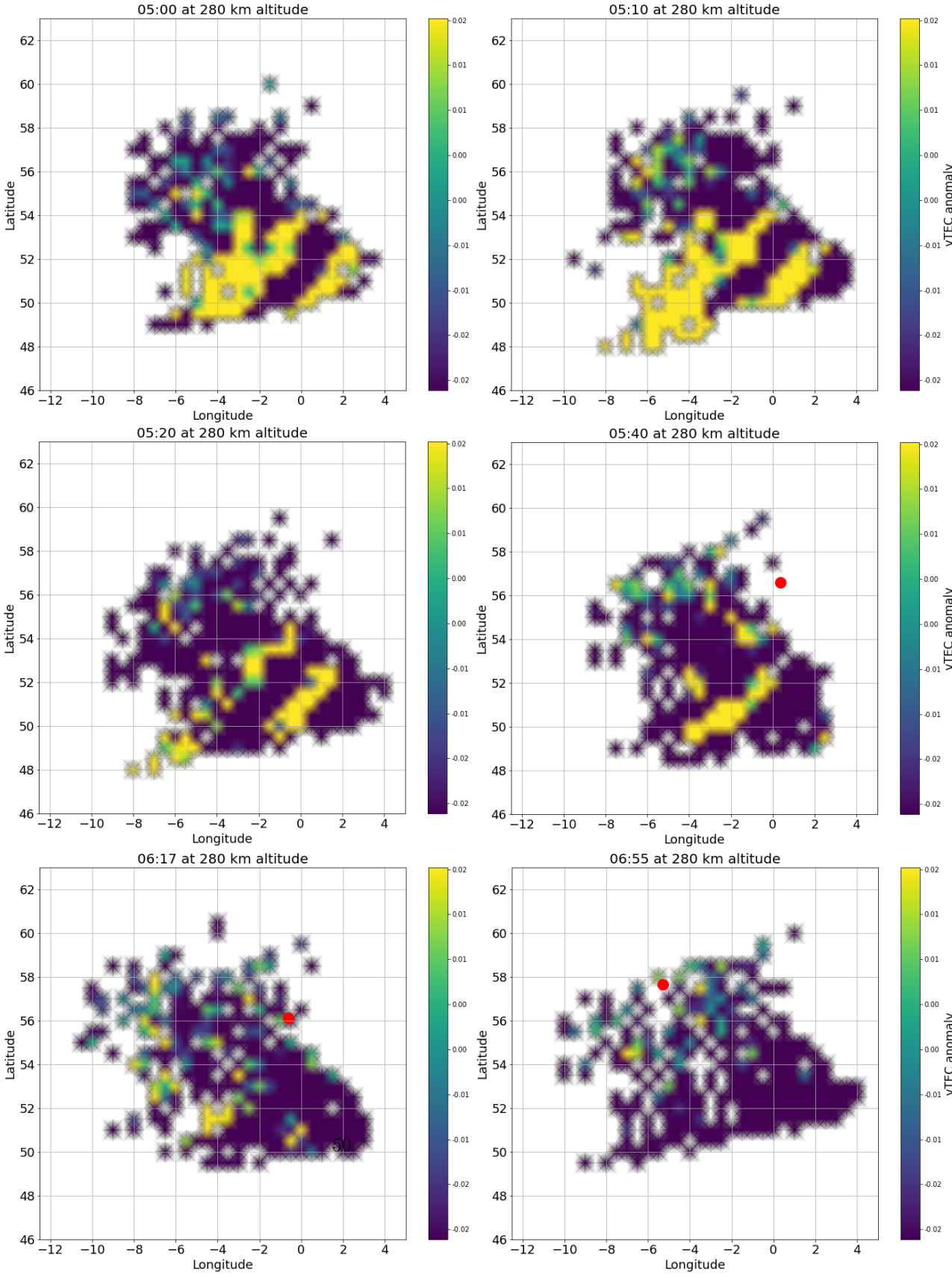
05:00 at 280 km altitude
05:10 at 280 km altitude
05:20 at 280 km altitude
05:40 at 280 km altitude
06:17 at 280 km altitude
06:55 at 280 km altitude
Latitude
Longitude
VTEC anomaly
50

10

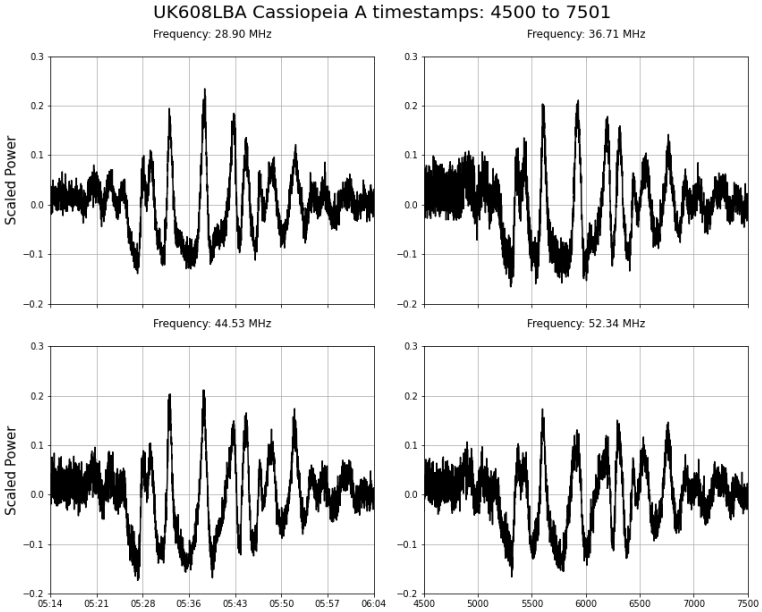
UK608LBA Cassiopeia A timestamps: 4500 to 7501
Frequency: 28.90 MHz
Frequency: 36.71 MHz
Frequency: 44.53 MHz
Frequency: 52.34 MHz
Scaled Power
Scaled Power
05:14
05:21
05:28
05:36
05:43
05:50
05:57
06:04
4500
5000
5500
6000
6500
7000
7500

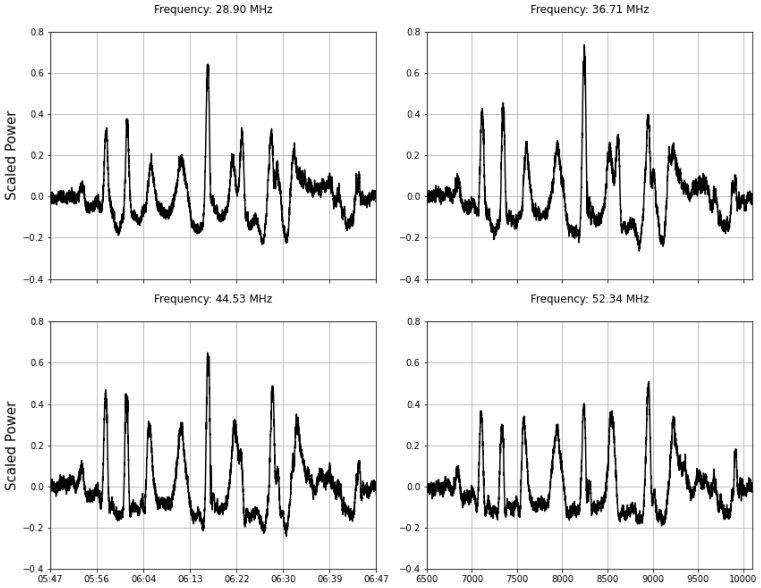
IE613LBA Cygnus A timestamps: 6500 to 10101
Frequency: 28.90 MHz
Frequency: 36.71 MHz
Frequency: 44.53 MHz
Frequency: 52.34 MHz
Scaled Power
Scaled Power
05:47
05:56
06:04
06:13
06:22
06:30
06:39
06:47
6500
7000
7500
8000
8500
9000
9500
10000

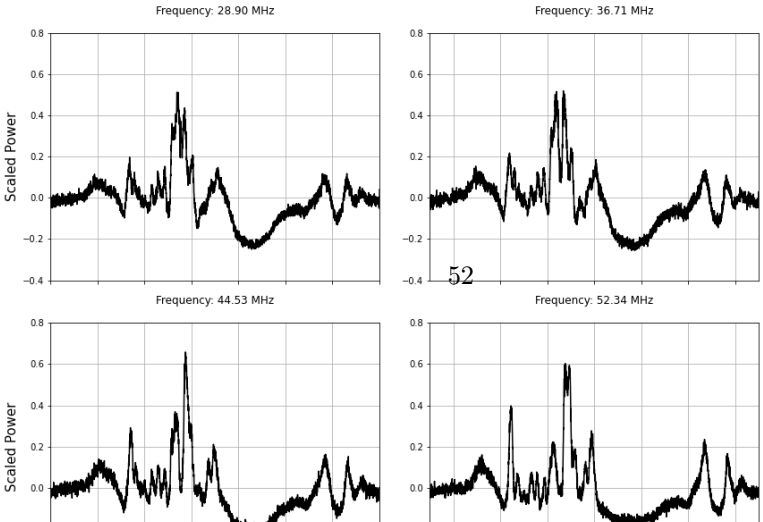
IE613LBA Cassiopeia A timestamps: 8750 to 12251
Frequency: 28.90 MHz
Frequency: 36.71 MHz
Frequency: 44.53 MHz
Frequency: 52.34 MHz
Scaled Power
Scaled Power

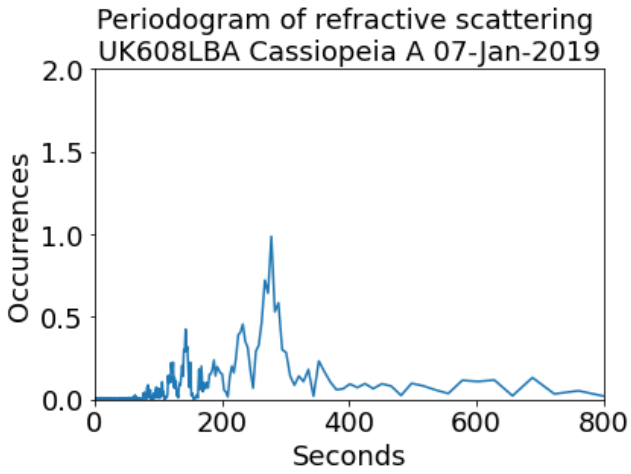
Periodogram of refractive scattering
UK608LBA Cassiopeia A 07-Jan-2019
Occurrences
Seconds
0.0
0.5
1.0
1.5
2.0
0
200
400
600
800

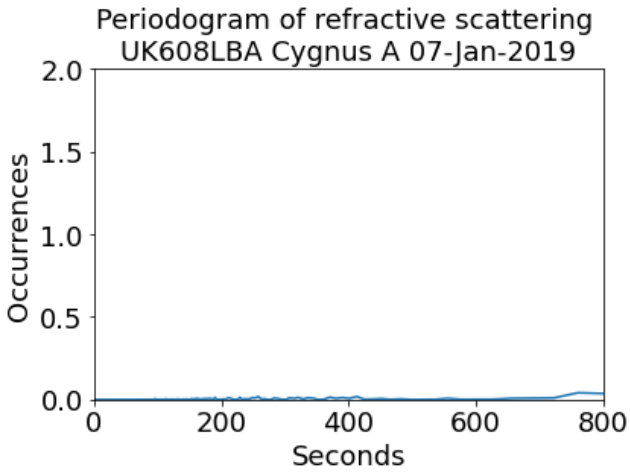
Periodogram of refractive scattering
UK608LBA Cygnus A 07-Jan-2019
Occurrences
Seconds
0.0
0.5
1.0
1.5
2.0
0
200
400
600
800

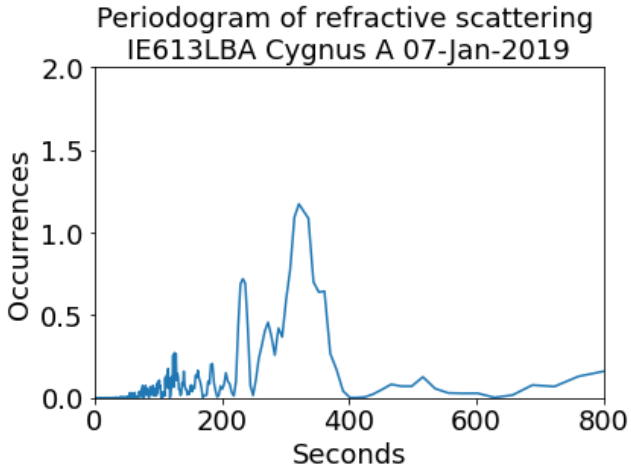
Periodogram of refractive scattering
IE613LBA Cygnus A 07-Jan-2019
Occurrences
Seconds
0.0
0.5
1.0
1.5
2.0
0
200
400
600
800

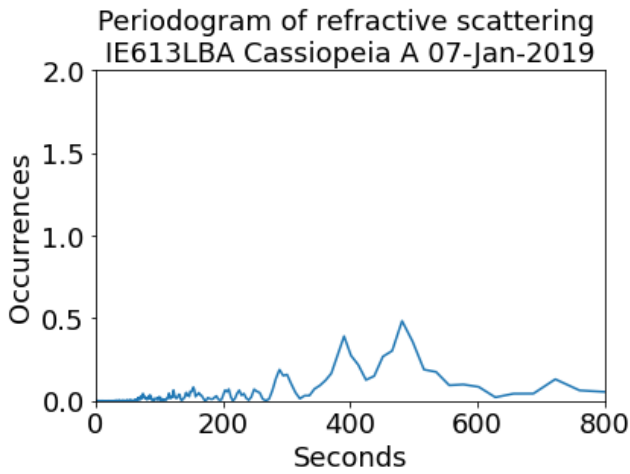
Periodogram of refractive scattering
IE613LBA Cassiopeia A 07-Jan-2019
Occurrences
Seconds
0.0
0.5
1.0
1.5
2.0
0
200
400
600
800

12